Supporting Information

Solvation-Engineered Two-Electron Viologen and TEMPO for Neutral Aqueous Organic Redox Flow Batteries

Yang Li,[a] Haozhe Xi,[a] Ruilin Wang,[b] Yu-Mo Zhang[a]*

[a] State Key Laboratory of Supramolecular Structure and Materials, College of Chemistry, Jilin University, Changchun, 130012, China

[b] College of Chemistry and Life Sciences, Advanced Institute of Materials Science, Changchun University of Technology, Changchun, 130012, China

Corresponding authors: zhangyumo@jlu.edu.cn.

The file includes:

1. Experimental Procedures

1.1 General information

2,2′-dibromo diethyl ether, trimethylamine (TMA, 2.0 mol L^{-1} in THF), 4,4′-bipyridine, 4-hydroxy-2,2,6,6-tetramethylpiperidin-1-oxyl (TEMPO-OH), tetrabutylammonium bromide (TBAB), 1,5-dibromopentane, and phenylhydrazine were purchased from Energy Chemical (Shanghai, China). Sodium hydroxide (NaOH), sodium chloride (NaCl), potassium chloride (KCl), ethanol (EtOH), toluene, and *N,N*-dimethylformamide (DMF) were obtained from Sinopharm Chemical Reagent Co., Ltd. Methyl tert-butyl ether (MTBE), acetonitrile (MeCN), petroleum ether (PE), ethyl acetate (EtOAc), and the Amberlite IRA-900 anion-exchange resin (chloride form, Adamas) were purchased from Titan Scientific Co., Ltd. Unless otherwise specified, all reagents were used as received without further purification.

1.2 Instrumental methods

UV-vis absorption spectra were recorded on a Shimadzu UV-2600i double-beam spectrophotometer. Electrochemical measurements were carried out using a BioLogic electrochemical workstation. Rotating disk electrode (RDE) experiments were performed on an electrochemical system from PINE Research (USA). ^{1}H and ^{13}C NMR spectra were acquired on a Zhongke Niujin AS400M NMR spectrometer, with tetramethylsilane (TMS) used as the internal standard for chemical shift calibration. Liquid chromatography-high-resolution mass spectrometry (LC-HRMS) analyses were conducted on an Agilent 1290-microTOF-Q II mass spectrometry system. Unless otherwise noted, all measurements were performed at room temperature.

1.3 Electrochemical Measurements

Electrodes were polished sequentially using alumina powders with particle sizes of 300 nm and 50 nm (Al_2O_3) prior to electrochemical measurements. After polishing, the glassy carbon electrode (geometric area: 0.707 cm^2) and the glassy carbon rotating disk electrode (geometric area: 0.196 cm^2) were ultrasonically cleaned with deionized water and dried under a nitrogen stream. The platinum counter electrode was flame-treated with an alcohol lamp before use to remove surface impurities. All electrochemical experiments were conducted in a conventional three-electrode configuration, employing a glassy carbon working electrode, a platinum coil counter electrode, and an Ag/AgCl reference electrode (saturated KCl). Unless otherwise noted, all measurements were performed at room temperature.

Preparation of Solutions for Cyclic Voltammetry (CV) and Determination of Diffusion Coefficients (*D*)

Solutions containing 4.0 mM redox-active species in 2.0 M NaCl were prepared to verify the success of the anion-exchange process. In addition, solutions containing 1.0 mM redox-active species in 1.0 M NaCl were prepared for cyclic voltammetry (CV) measurements at various scan rates. All electrochemical experiments were conducted under a nitrogen atmosphere at 298 K. CV measurements of BTTAE-V-Cl and TMEE-TEMPO-Cl were performed over a scan-rate range of 100–5000 mV s^{-1}. The diffusion coefficients (*D*) of both compounds were determined using the Randles–Ševčík equation (Equation 1, for reversible systems). In this equation, i_p is the peak current (A), *n* is the number of electrons transferred, *A* is the effective electrode area (0.707 cm^2), *C* is the bulk concentration (mol·cm^{-3}), *D* is the diffusion coefficient (cm^2 s^{-1}), and v is the scan rate (V s^{-1}).

$$I_p = 2.69 \times 10^5 n^{\frac{3}{2}} A C D^{\frac{1}{2}} v^{\frac{1}{2}} \qquad (Equation\ 1)$$

Rotating Disk Electrode (RDE) Measurements

A 1.0 mM solution of the redox-active species containing 1.0 M NaCl as the supporting electrolyte was prepared for rotating disk electrode (RDE) experiments. A glassy carbon rotating disk electrode (RDE) was used as the working electrode, a platinum wire served as the counter electrode, and an Ag/AgCl (saturated KCl) electrode was used as the reference electrode. Prior to each measurement, the working electrode was polished sequentially with 0.3 μm and 0.05 μm alumina slurries, followed by ultrasonic cleaning in deionized water and drying under a nitrogen stream. All measurements were performed at 298 K under a nitrogen atmosphere. The rotation rates were set to 225, 400, 625, 900, 1225, 1600, and 2025 rpm, and the scan rate was 5 mV s^{-1}. In RDE experiments, the measured current is governed by mass-transport limitations and can be described by the Koutecký–Levich equation (Equation 2), where *i* is the measured current, i_k is the kinetic current, and i_{lim} is the diffusion-limited current. According to the Levich equation (Equation 3), *n* is the number of electrons transferred, F is the Faraday constant (96,485 C·mol^{-1}), *A* is the electrode area (0.196 cm^2), *C* is the bulk concentration of electroactive species (mol·cm^{-3}), *D* is the diffusion coefficient (cm^2 s^{-1}), *v* is the kinematic viscosity of the electrolyte (9.56×10^{-3} cm^2 s^{-1} for 1.0 M NaCl), and ω is the angular rotation rate (rad s^{-1}). To determine the diffusion-limited current for the second reduction step, the limiting current of the first reduction step was subtracted from the total current. A Koutecký–Levich plot was constructed by plotting $1/i_{lim}$ versus $\omega^{-1/2}$ at different

rotation rates, and the diffusion coefficient D was obtained from the slope of the linear fit. Once the diffusion-limited current was determined, the kinetic current i_k was calculated using the Koutecký–Levich equation. The Tafel equation (Equation 4) describes the kinetic region of the electrode reaction, where i_k is the kinetic current, k_0 is the heterogeneous electron-transfer rate constant (cm s^{-1}), α is the charge-transfer coefficient, η is the overpotential, R is the gas constant (8.314 J·mol^{-1} K^{-1}), and T is the absolute temperature (K). The exchange current density (i_0) was obtained from extrapolation of the Tafel plot to zero overpotential. According to the Butler–Volmer equation (Equation 5), the heterogeneous electron-transfer rate constant (k_0) was calculated from the exchange current i_0.

$$\frac{1}{i} = \frac{1}{i_k} + \frac{1}{i_{lim}} \qquad (Equation\ 2)$$

$$i_{lim} = 0.620n\mathrm{F}ACD^{\frac{2}{3}}v^{-\frac{1}{6}}\omega^{\frac{1}{2}} \qquad (Equation\ 3)$$

$$\log(i_k) = \log(n\mathrm{F}ACk_0) + \frac{\alpha n\mathrm{F}\eta}{2.303\mathrm{RT}} \qquad (Equation\ 4)$$

$$i_0 = n\mathrm{F}Ak_0C \qquad (Equation\ 5)$$

1.4 Solubility measurements

Calibration curves for the redox-active electrolytes were established using UV-vis spectrophotometry. A series of standard solutions with known concentrations was prepared, and their absorbances were recorded at the corresponding characteristic absorption wavelength (λ_{max}). The resulting linear relationship between absorbance and concentration was used for subsequent quantitative analysis. To determine solubility, an excess amount of the redox-active electrolyte (beyond its solubility limit) was added to deionized water or to a 2.0 M NaCl aqueous solution. The suspensions were heated and sonicated to facilitate dissolution, followed by equilibration at room temperature. After standing to reach saturation, the mixtures were filtered through a 0.45 μm microporous membrane to remove undissolved solids, affording the saturated solutions. Aliquots of the saturated solutions were appropriately diluted, and their absorbances were measured at λ_{max}. The electrolyte concentrations were then calculated from the established calibration curves. These concentrations were taken as the solubility values in the corresponding media. All solubility measurements were performed at 25 °C.

1.5 DFT calculations

Density functional theory (DFT) calculations were carried out using the Gaussian 16 program package. Geometry optimizations and vibrational frequency analyses were performed at the B3LYP/6-311+G(d,p) level of theory. Solvent effects of water were described using the SMD implicit solvation model. Grimme's D3 dispersion correction with Becke–Johnson damping (GD3BJ) was applied to account for dispersion interactions. All calculations were performed without symmetry constraints. Frequency calculations were conducted for all optimized structures to confirm that they correspond to true minima on the potential energy surface, as evidenced by the absence of imaginary frequencies. The obtained Gibbs free energies were used for subsequent thermodynamic analysis. Electrostatic potential (ESP) distributions were analyzed based on the optimized geometries using the Multiwfn program, and the ESP surfaces were visualized with VMD. The electrostatic potential was mapped onto the electron density surface to evaluate the surface charge distribution of the molecules. Solvation free energies (ΔG_solv) were obtained from the Gibbs free energy difference between the solution-phase and gas-phase calculations based on the optimized geometries.

1.6 Permeability measurements

The crossover behavior of the active species was evaluated using a two-compartment diffusion cell separated by a commercial Selemion DSV anion-exchange membrane. Prior to the measurement, the membrane was soaked in 2.0 M NaCl aqueous solution for at least 24 h to ensure full hydration and ionic equilibration.

For the permeability measurement, 10 mL of 0.1 M BTTAE-V-Cl (or 0.2 M TMEE-TEMPO-Cl) dissolved in 1.6 M NaCl aqueous solution was introduced into the donating compartment, while the receiving compartment was filled with 10 mL of 2.0 M NaCl aqueous solution to maintain ionic balance. Both compartments were continuously stirred to minimize concentration polarization.

At predetermined time intervals, small aliquots were withdrawn from the receiving side and diluted with 2.0 M NaCl electrolyte. The concentrations of the active species were determined using UV–vis spectroscopy according to the calibration curves shown in Fig. S21 and Fig. S26. The permeability coefficient P was calculated according to the following equation:

$$P = -\frac{V_0 L}{2At} ln(1 - \frac{2C_t}{C_0})$$

where P is the permeability coefficient ($cm^2\ s^{-1}$), C_t is the concentration in the receiving compartment at time t, C_0 is the initial concentration in the donor compartment, V_0 (10 mL) is

the electrolyte volume, L (100 μm) is the membrane thickness, and A (0.7854 cm^2) is the effective membrane area.

1.7 Theoretical Energy Density and Capacity Calculations

The theoretical energy density of the BTTAE-V-Cl/TMEE-TEMPO-Cl AORFB is calculated using the equation (Equation 6):

$$\mathrm{E}_{theoretical}\left(\frac{Wh}{L}\right)=\frac{nCFV}{\mu_v} \qquad \text{(Equation 6)}$$

where n is the number of electrons involved in the cell reaction, C is the concentration of active materials, F is Faraday′s constant 26.8 Ah mol^{-1}, V is the cell voltage, μ_v is the volume factor (μ_v = 1 + lower electrolyte concentration/higher electrolyte concentration). For BTTAE-V-Cl/TMEE-TEMPO-Cl AORFB,

$$\mu_v = 1 + 1.55/3.3 = 1.47,$$

and the theoretical energy density is calculated as

$$\mathrm{E}_{\mathrm{theoretical}} = (1 \times 1.56 \times 26.8 \times \frac{1.55}{1.47}) + (1 \times 1.22 \times 26.8 \times \frac{1.55}{1.47}) = 78.0\ Wh\ L^{-1}.$$

The theoretical volumetric density of the BTTAE-V-Cl/TMEE-TEMPO-Cl AORFB is calculated using the equation (Equation 7):

$$\text{Theoretical volumetric capacity} = 26.806 \times nC\ (\text{Ah L}^{-1}) \qquad \text{(Equation 7)}$$

where n is the number of electrons transferred per molecule, C is the molecular concentration (M). As the capacity-limiting side is the BTTAE-V-Cl anolyte, n is 2 and C is the concentration of BTTAE-V-Cl.

1.8 Aqueous Organic Redox Flow Battery Testing

The flow battery components were purchased from Wuhan Zhisheng New Energy. The cell assembly consisted of two graphite flow-field plates featuring serpentine flow channels, with carbon felt (effective electrode area: 25 cm^2) used as the electrode material. A DSV membrane (Japan, thickness of 100 μm) served as the ion-exchange separator. The electrolytes were continuously circulated using a peristaltic pump (DIPump 550, Kamoer Fluid Tech (Shanghai) Co., Ltd.) at a rotational speed corresponding to 69 rpm. After assembly, the electrolyte reservoirs were purged with high-purity nitrogen (99.999%) to remove dissolved oxygen, and the entire system was subsequently sealed. The oxygen concentration was monitored in real time using an inline oxygen sensor and maintained within the range of 50–500 ppm during

operation. If the oxygen level exceeded 500 ppm, nitrogen purging was performed again to displace residual oxygen. All flow battery tests were conducted at 283 K.

Preparation of Electrolyte Solutions

The anolyte was prepared by dissolving BTTAE-V-Cl in a 2.0 M NaCl aqueous solution to obtain a final concentration of 0.10 mol L^{-1}. The catholyte was prepared by dissolving TMEE-TEMPO-Cl in a 2.0 M NaCl aqueous solution to a final concentration of 0.20 mol L^{-1}. The electrolyte volume on each side was set to either 10 mL or 15 mL, depending on the experimental requirements. All solutions were prepared using deionized water and purged with nitrogen prior to use to remove dissolved oxygen.

High-concentration electrolyte preparation

For high-concentration battery tests, the anolyte was prepared by dissolving BTTAE-V-Cl in a 2.0 M NaCl aqueous solution to obtain a final concentration of 0.50 mol L^{-1}. The catholyte was prepared by dissolving TMEE-TEMPO-Cl in a 2.0 M NaCl aqueous solution to a final concentration of 1.00 mol L^{-1}. The electrolyte volumes on both sides were maintained at 10 mL unless otherwise specified. All solutions were prepared using deionized water and were purged with nitrogen prior to use to remove dissolved oxygen.

Flow Battery Testing Conditions

Flow battery performance was evaluated using a LANHE battery testing system (CT2001B). For electrolyte volumes of 10 mL, the charge-discharge voltage window was set to 0.1–1.8 V, while for 15 mL electrolyte systems, the voltage window was adjusted to 0.1–1.7 V. Long-term galvanostatic cycling was conducted at a current density of 40 mA cm^{-2}. Prior to the formal cycling tests, 1–2 preconditioning charge-discharge cycles were performed to ensure stabilization of the electrode–electrolyte system.

Galvanostatic–potentiostatic (GP) cycling test at moderate concentration

For the moderate-concentration system, the anolyte consisted of 0.10 M BTTAE-V-Cl and the catholyte consisted of 0.20 M TMEE-TEMPO-Cl, both dissolved in 2.0 M NaCl aqueous supporting electrolyte. Unless otherwise specified, the electrolyte volume on each side was 15 mL. Galvanostatic–potentiostatic (GP) cycling tests were performed using a two-step charging protocol. The cell was first charged galvanostatically at a current density of 20 mA cm^{-2} until reaching a cutoff voltage of 1.75 V, followed by a potentiostatic step at 1.75 V until the current

decreased to 1 mA cm^{-2}. Discharge was conducted galvanostatically to a cutoff voltage of 0.15 V.

Asymmetric cell configurations for decoupled stability evaluation

For the catholyte-limited configuration, the anolyte consisted of 0.30 M BTTAE-V-Cl (30 mL) and the catholyte consisted of 0.10 M TMEE-TEMPO-Cl (15 mL), both dissolved in 2.0 M NaCl supporting electrolyte. Under this condition, the cell capacity is governed by the one-electron redox process of TMEE-TEMPO-Cl. Galvanostatic cycling was performed at a current density of 40 mA cm^{-2} within a voltage window of 0.10–1.80 V.

For the anolyte-limited configuration, the anolyte consisted of 0.10 M BTTAE-V-Cl (15 mL) and the catholyte consisted of 0.40 M TMEE-TEMPO-Cl (30 mL) in 2.0 M NaCl supporting electrolyte. In this configuration, the overall capacity is governed by the viologen redox process. Galvanostatic cycling was conducted at 40 mA cm^{-2} within a voltage window of 0.15–1.80 V.

1.9 Synthesis of molecules

Synthesis route of BTTAE-V-Cl

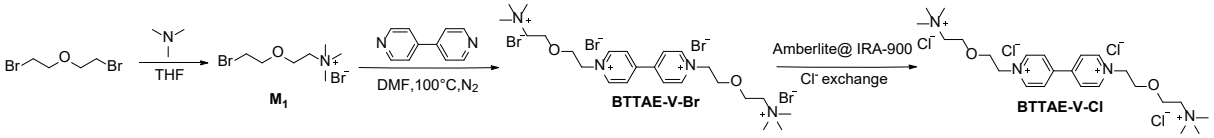

Figure S1 Synthesis route of BTTAE-V-Cl.

Synthesis of M_1

A solution of 2,2′-dibromo diethyl ether (1.25 mL, 10.0 mmol, 1.0 equiv.) and trimethylamine in THF (2.0 mol L^{-1}, 5.0 mL, 10.0 mmol, 1.0 equiv.) was added sequentially to a 10 mL round-bottom flask and stirred at room temperature for 10 h. Upon completion, the resulting solid was collected by vacuum filtration, washed with methyl tert-butyl ether (MTBE) three times, and dried under vacuum to afford the target product M_1 as a white solid (yield: 72%). ^{1}H NMR (400 MHz, Deuterium Oxide) δ 4.05 (dq, J = 7.4, 2.7 Hz, 2H), 3.97–3.92 (m, 2H), 3.68–3.63 (m, 4H), 3.25 (s, 9H). ^{13}C NMR (101 MHz, Deuterium Oxide) δ 70.67, 65.35, 64.21, 54.11, 31.37. LC-HRMS (ESI) Calc. for $C_7H_{17}BrNO^+$: 210.0489, Found: 210.0488.

Synthesis of BTTAE-V-Br and BTTAE-V-Cl

A mixture of M1 (1.98 g, 6.85 mmol, 3.0 equiv), 4,4′-bipyridine (0.36 g, 2.27 mmol, 1.0 equiv), and DMF (15 mL) was added sequentially to a 25 mL round-bottom flask. The reaction was carried out under a nitrogen atmosphere and stirred at 100 °C in an oil bath. As the reaction

proceeded, the initially milky-white suspension turned clear, followed by the formation of a large amount of yellow precipitate. The reaction progress was monitored by thin-layer chromatography. After 48 h, the resulting solid was collected by filtration, washed with DMF three times and subsequently with CH_3CN three times, and dried under vacuum to afford BTTAE-V-Br as a yellow solid (87% yield). BTTAE-V-Br (1.50 g, 2.04 mmol) was then dissolved in deionized water (20 mL) and subjected to anion-exchange column chromatography using Amberlite® IRA-900 anion-exchange resin (30.0 g). The ion-exchange procedure was repeated twice to ensure complete replacement of the bromide anion. The resulting aqueous solution was concentrated by rotary evaporation and dried under vacuum to afford BTTAE-V-Cl (88% yield). ^{1}H NMR (400 MHz, Deuterium Oxide) δ 9.17 (d, J = 6.8 Hz, 4H), 8.62 (d, J = 6.8 Hz, 4H), 5.03–4.96 (m, 4H), 4.17–4.10 (m, 4H), 3.99 (dq, J = 7.6, 2.7 Hz, 4H), 3.65–3.58 (m, 4H), 3.16 (s, 18H). ^{13}C NMR (101 MHz, Deuterium Oxide) δ 150.40, 146.03, 127.05, 68.65, 65.62, 64.63, 61.52, 54.82.

Synthesis route of TMEE-TEMPO-Cl

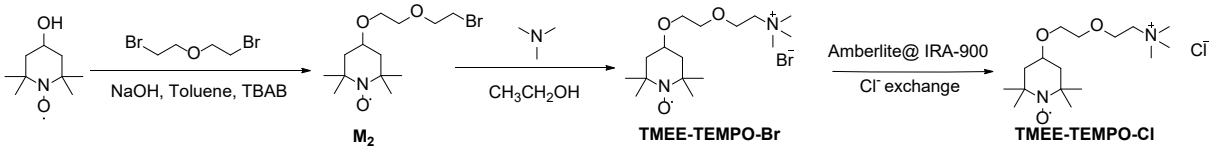

Figure S2 Synthesis route of TMEE-TEMPO-Cl.

Synthesis of M_2

4-OH-TEMPO (1.74 g, 10.1 mmol, 1.0 equiv), tetrabutylammonium bromide (TBAB, 0.39 g, 1.2 mmol), and 2,2′-dibromo-diethyl ether (2.15 mL, 17.26 mmol, 1.7 equiv) were sequentially added to a biphasic mixture of toluene (4.5 mL) and 50% aqueous NaOH (15 mL). The reaction mixture was vigorously stirred at room temperature. The reaction progress was monitored by thin-layer chromatography, and the reaction reached completion after approximately 48 h. Upon completion, 150 mL of methyl tert-butyl ether (MTBE) was added and the mixture was extracted several times with deionized water (100 mL). The combined organic layers were dried over anhydrous Na_2SO_4, and the solvent was removed under reduced pressure to afford the red solid product M_2 in 72% yield. The synthesized M_2 was subjected to ^{1}H NMR analysis after reduction with phenylhydrazine. ^{1}H NMR (400 MHz, DMSO-d_6) δ 3.73 (t, J = 5.8 Hz, 2H), 3.59–3.56 (m, 3H), 3.55–3.50 (m, 4H), 1.91–1.82 (m, 2H), 1.26–1.21 (m, 2H), 1.05 (d, J = 12.1 Hz, 12H). LC-HRMS (ESI) Calc. for $C_{13}H_{23}BrNO_3^{\cdot}$: 322.1018. Found: 322.1015.

Synthesis of TMEE-TEMPO-Br and TMEE-TEMPO-Cl

Compound M_2 (4.10 g, 12.7 mmol, 1.0 equiv) and 70.0 mL of a trimethylamine ethanol solution (2.0 mol L^{-1} in ethanol, 140.0 mmol, 11.0 equiv) were added to a 100 mL round-bottom flask and stirred at room temperature. The reaction progress was monitored by thin-layer chromatography, and the reaction reached completion after 48 h. The reaction mixture was concentrated under reduced pressure, and the resulting viscous residue was dissolved in deionized water (50 mL). The aqueous layer was extracted multiple times with methyl tert-butyl ether (MTBE, 100 mL). The combined aqueous phases were collected and dried to afford the red solid TMEE-TEMPO-Br in 78% yield. TMEE-TEMPO-Br (1.55 g, 4.07 mmol) was dissolved in deionized water (20.0 mL) and subjected to anion exchange using Amberlite® IRA-900 anion-exchange resin (31 g). The exchange process was repeated twice to ensure complete anion substitution. The resulting solution was concentrated by rotary evaporation to remove water, yielding the red solid TMEE-TEMPO-Cl in 93% yield. The synthesized TMEE-TEMPO-Cl was analyzed by ^{1}H NMR spectroscopy after reduction with phenylhydrazine. ^{1}H NMR (400 MHz, DMSO-d_6) δ 3.83 (dt, J = 5.2, 2.5 Hz, 2H), 3.60–3.50 (m, 7H), 3.11 (s, 9H), 1.87–1.81 (m, 2H), 1.26–1.21 (m, 2H), 1.05 (d, J = 12.4 Hz, 12H). LC-HRMS (ESI) Calc. for $C_{16}H_{34}N_2O_3^{\bullet+}$: 302.2564. Found: 302.2568.

Synthesis of BBrEE

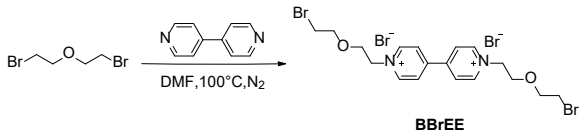

Figure S3 Synthesis route of BBrEE.

A mixture of 2,2′-dibromo-diethyl ether (1.98 g, 8.6 mmol, 4.0 equiv), 4,4′-bipyridine (0.34 g, 2.18 mmol, 1.0 equiv), and DMF (10 mL) was added sequentially to a 25 mL round-bottom flask. The reaction was carried out under a nitrogen atmosphere and stirred at 100 °C in an oil bath. As the reaction proceeded, the initially milky-white suspension turned clear, followed by the formation of a large amount of yellow precipitate. The reaction progress was monitored by thin-layer chromatography. After 48 h, the resulting solid was collected by filtration, washed with DMF three times and subsequently with CH_3CN three times, and dried under vacuum to afford BBrEE as a yellow solid (35% yield). ^{1}H NMR (400 MHz, Deuterium Oxide) δ 9.10 (d, J = 6.9 Hz, 4H), 8.52 (d, J = 7.0 Hz, 4H), 4.92–4.85 (m, 4H), 4.07 (t, J = 4.9 Hz, 4H), 3.85–3.78 (m, 4H), 3.49–3.42 (m, 4H). ^{13}C NMR (101 MHz, Deuterium Oxide) δ 150.40, 146.16, 70.61, 68.34, 61.35, 31.59.

Synthesis route of TMAPE-V-Cl

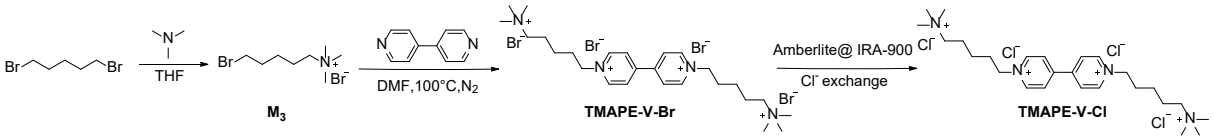

Figure S4 Synthesis route of TMAPE-V-Cl.

Synthesis of M_3

A mixture of 1,5-dibromopentane (1.36 mL, 10.0 mmol, 1.0 equiv) and a trimethylamine tetrahydrofuran solution (5.0 mL, 2.0 mol L^{-1} in THF, 10.0 mmol, 1.0 equiv) was added to a 25 mL round-bottom flask and stirred at room temperature. A substantial amount of white solid precipitated during the reaction. After stirring for 10 h, the solid was collected by vacuum filtration and washed three times with methyl tert-butyl ether (MTBE) to afford the desired product M_3 as a white powder in 89% yield. ^{1}H NMR (400 MHz, Deuterium Oxide) δ 3.51 (t, J = 6.6 Hz, 2H), 3.32 (dd, J = 10.6, 6.5 Hz, 2H), 3.10 (s, 9H), 1.95–1.87 (m, 2H), 1.86–1.76 (m, 2H) 1.50 (p, J = 7.6 Hz, 2H). ^{13}C NMR (101 MHz, Deuterium Oxide) δ 66.52, 53.07, 34.64, 31.54, 24.31, 21.72. LC-HRMS (ESI) Calc. for $C_8H_{17}BrN^+$: 208.0696. found: 208.0693.

Synthesis of TMAPE-V-Br and TMAPE-V-Cl

A mixture of M_3 (1.78 g, 6.20 mmol, 3.0 equiv) and 4,4′-bipyridine (0.32 g, 2.05 mmol, 1.0 equiv) was added to a 25 mL round-bottom flask containing 15 mL of DMF and heated at 100 °C in an oil bath under a nitrogen atmosphere. As the reaction proceeded, the initially white and turbid suspension gradually turned clear, followed by the formation of a large amount of yellow precipitate. The reaction progress was monitored by thin-layer chromatography, and completion was reached after 48 h. The resulting yellow solid was collected and washed sequentially with DMF and CH_3CN. After drying, the target product TMAPE-V-Br was obtained as a yellow solid in 91% yield. Subsequently, TMAPE-V-Br (1.55 g, 2.12 mmol) was dissolved in 20.0 mL of deionized water and subjected to anion exchange using Amberlite® IRA-900 resin (31.0 g). The ion-exchange procedure was repeated twice to ensure complete replacement of the anions. The resulting solution was concentrated by rotary evaporation to remove water, affording TMAPE-V-Cl as a purple-brown solid in 85% yield. ^{1}H NMR (400 MHz, Deuterium Oxide) δ 9.16 (d, J = 6.8 Hz, 4H), 8.59 (d, J = 6.7 Hz, 4H), 3.42–3.33 (m, 4H), 3.14 (s, 18H), 2.20 (p, J = 7.7 Hz, 4H), 1.91 (dq, J = 12.2, 8.3, 6.1 Hz, 4H), 1.51 (p, J = 7.8 Hz, 4H). ^{13}C NMR (101 MHz, Deuterium Oxide) δ 150.13, 145.50, 127.15, 66.08, 61.73, 52.91, 30.19, 22.32, 21.98.

2. Figure

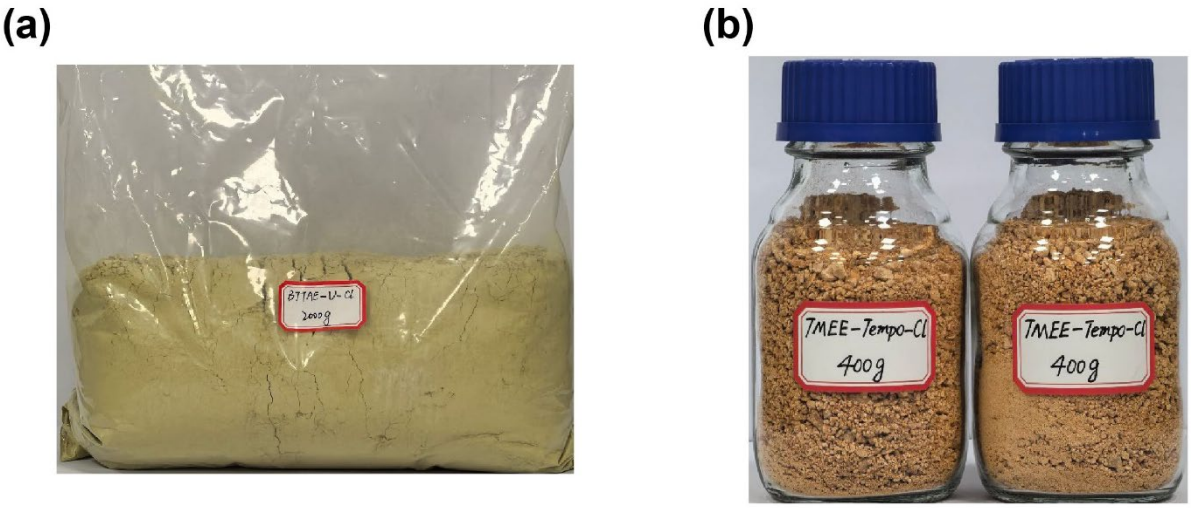

Figure S5 Photographs of the kilogram-scale synthesized active materials. (a) BTTAE-V-Cl anolyte. (b) TMEE-TEMPO-Cl catholyte.

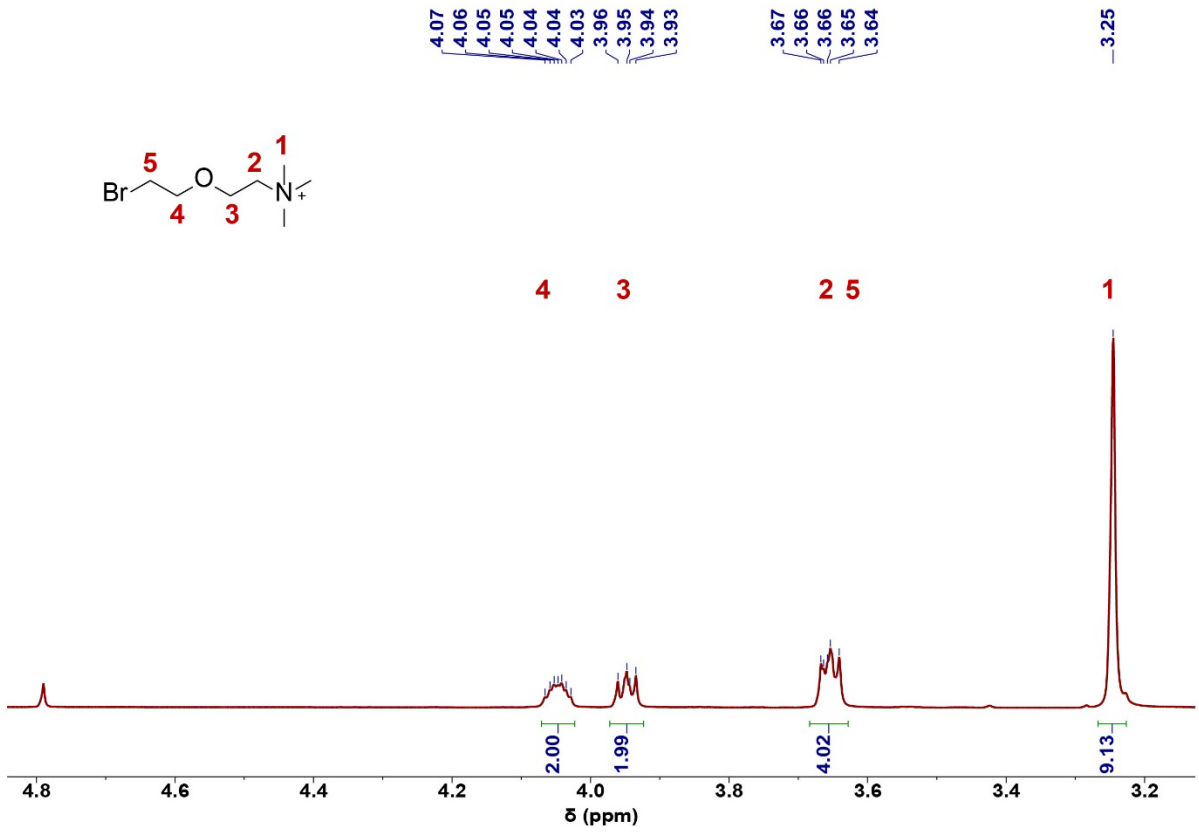

Figure S6 ^{1}H NMR spectrum of M_1, recorded in D_2O at 25 °C.

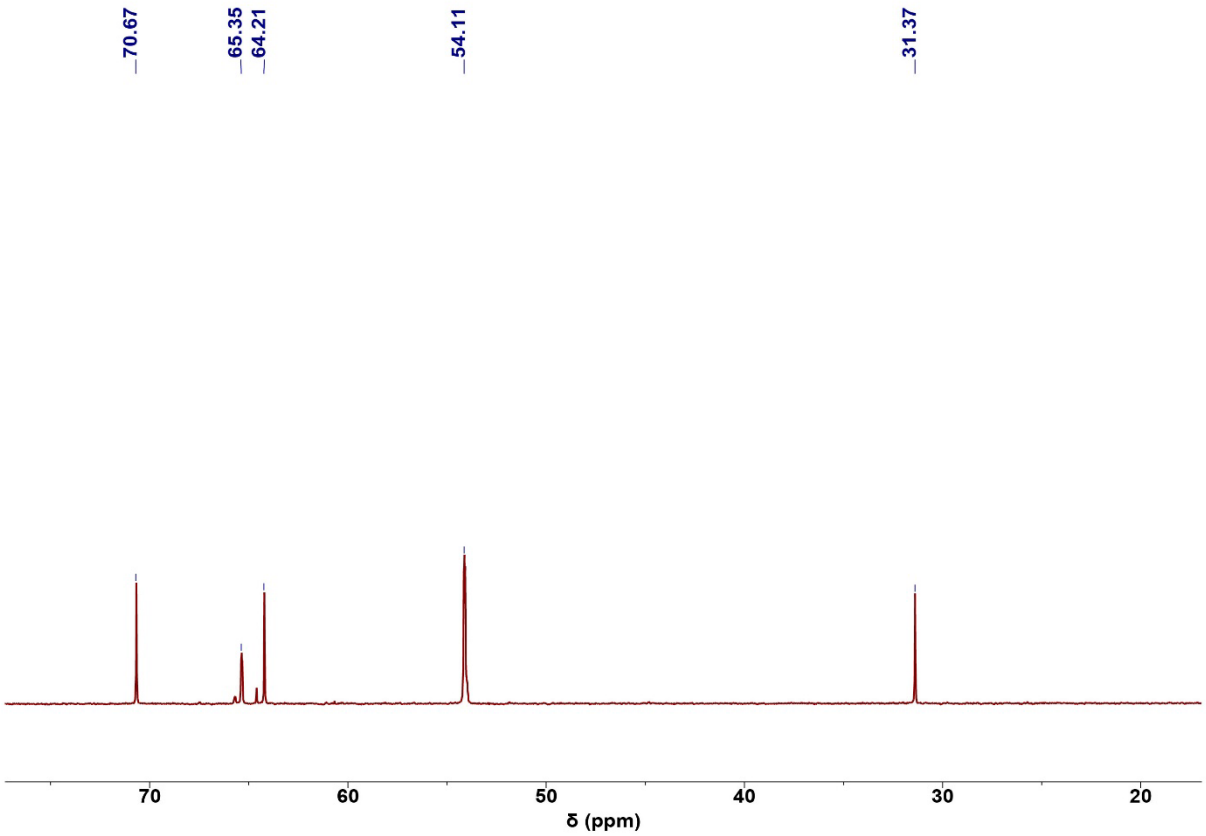

Figure S7 ^{13}C NMR spectrum of M_1, recorded in D_2O at 25 °C.

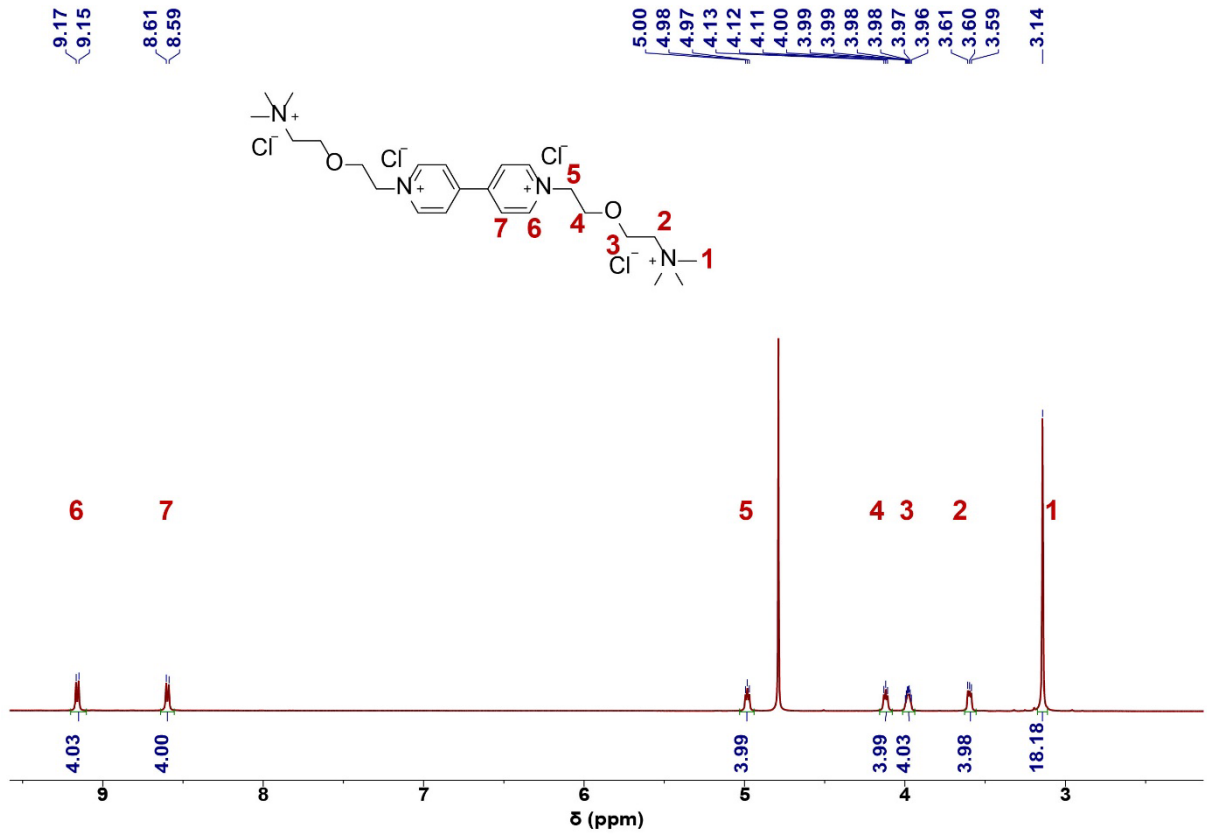

Figure S8 ^{1}H NMR spectrum of BTTAE-V-Cl, recorded in D_2O at 25 °C.

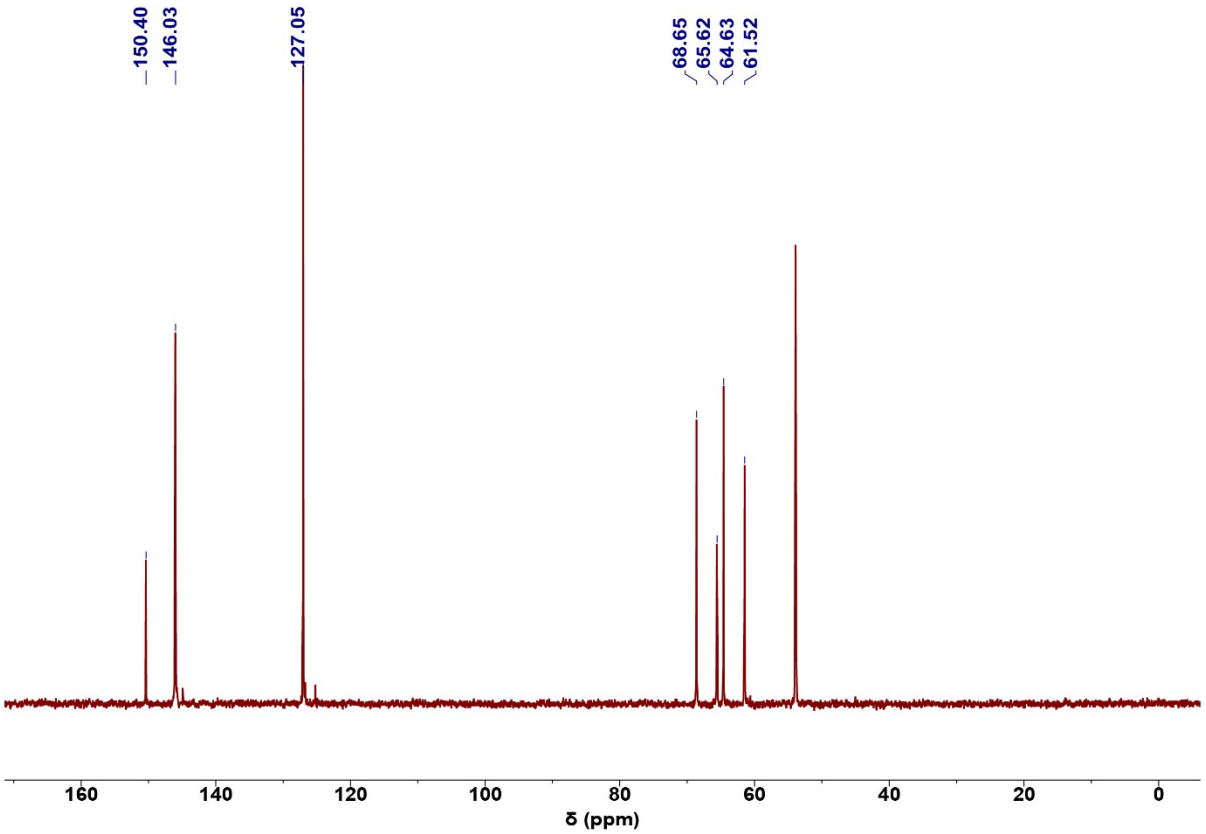

Figure S9 ^{13}C NMR spectrum of BTTAE-V-Cl, recorded in D_2O at 25 °C.

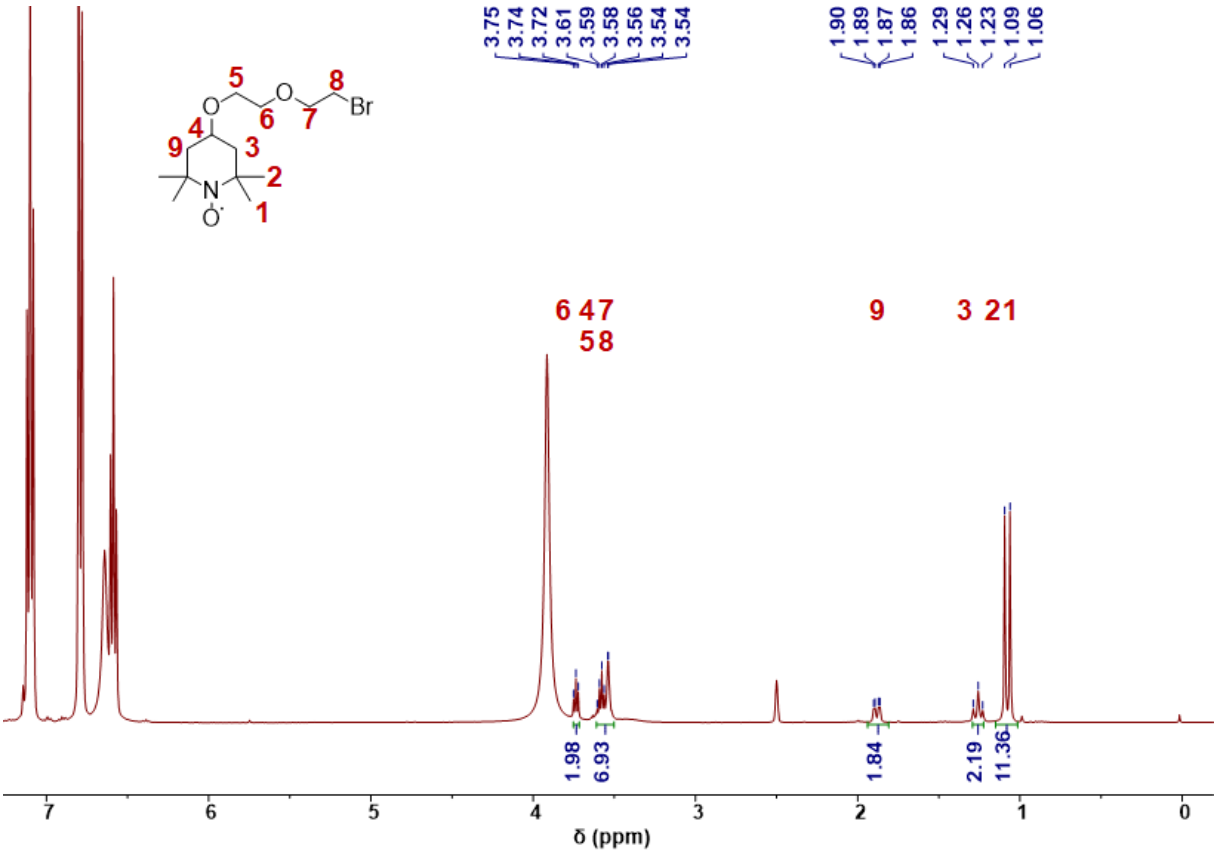

Figure S10 ^{1}H NMR spectrum of M_2, recorded in DMSO-d_6 at 25 °C. The signals that were not integrated correspond to phenylhydrazine and the NMR solvent.

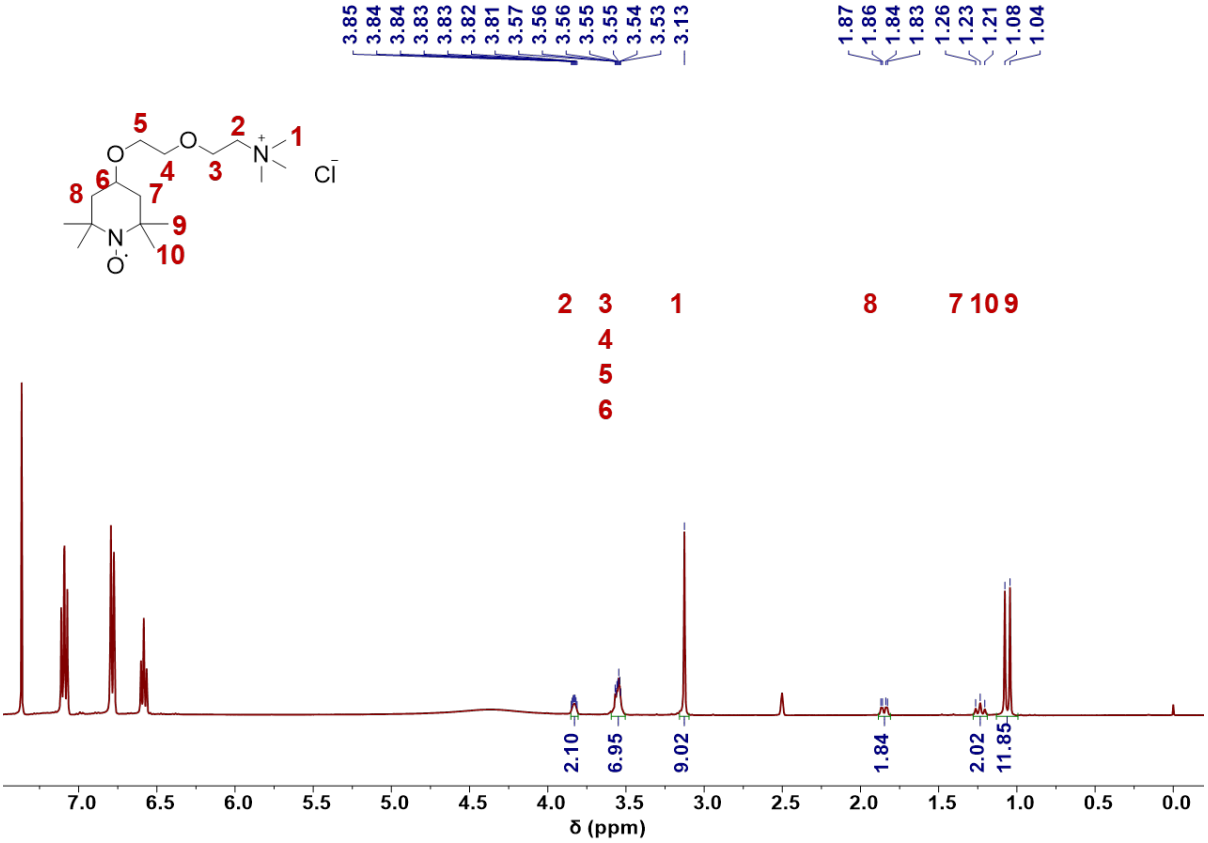

Figure S11 ^{1}H NMR spectrum of TMEE-TEMPO-Cl, recorded in DMSO-d_6 at 25 °C. The signals that were not integrated correspond to phenylhydrazine and the NMR solvent.

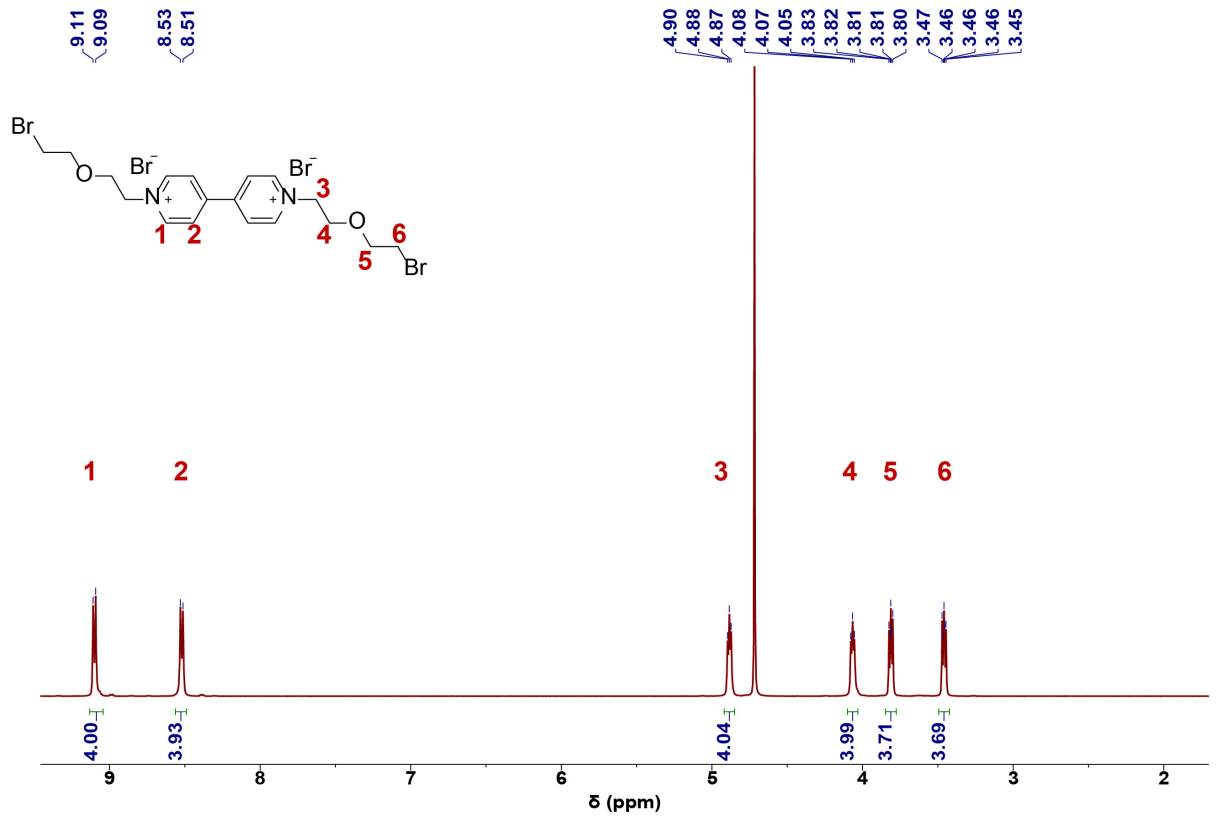

Figure S12 ^{1}H NMR spectrum of BBrEE, recorded in D_2O at 25 °C.

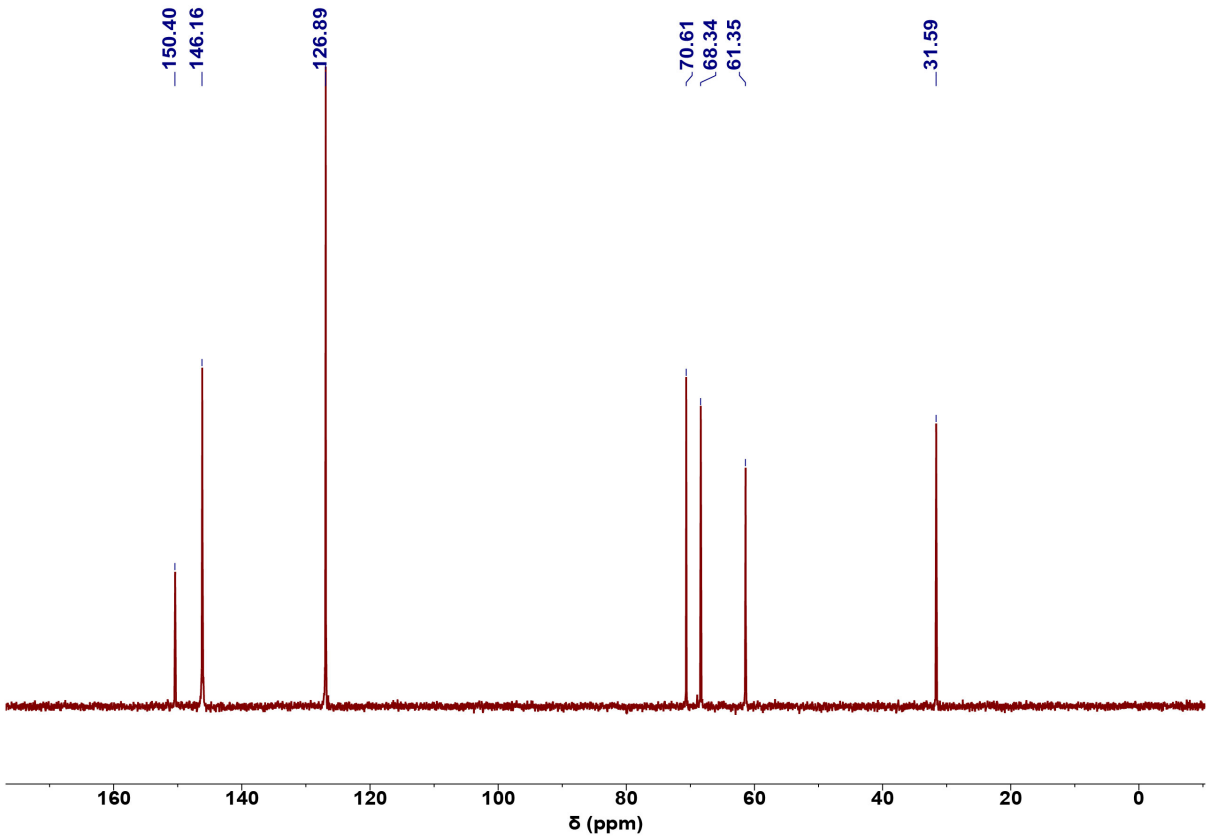

Figure S13 ^{13}C NMR spectrum of BBrEE, recorded in D_2O at 25 °C.

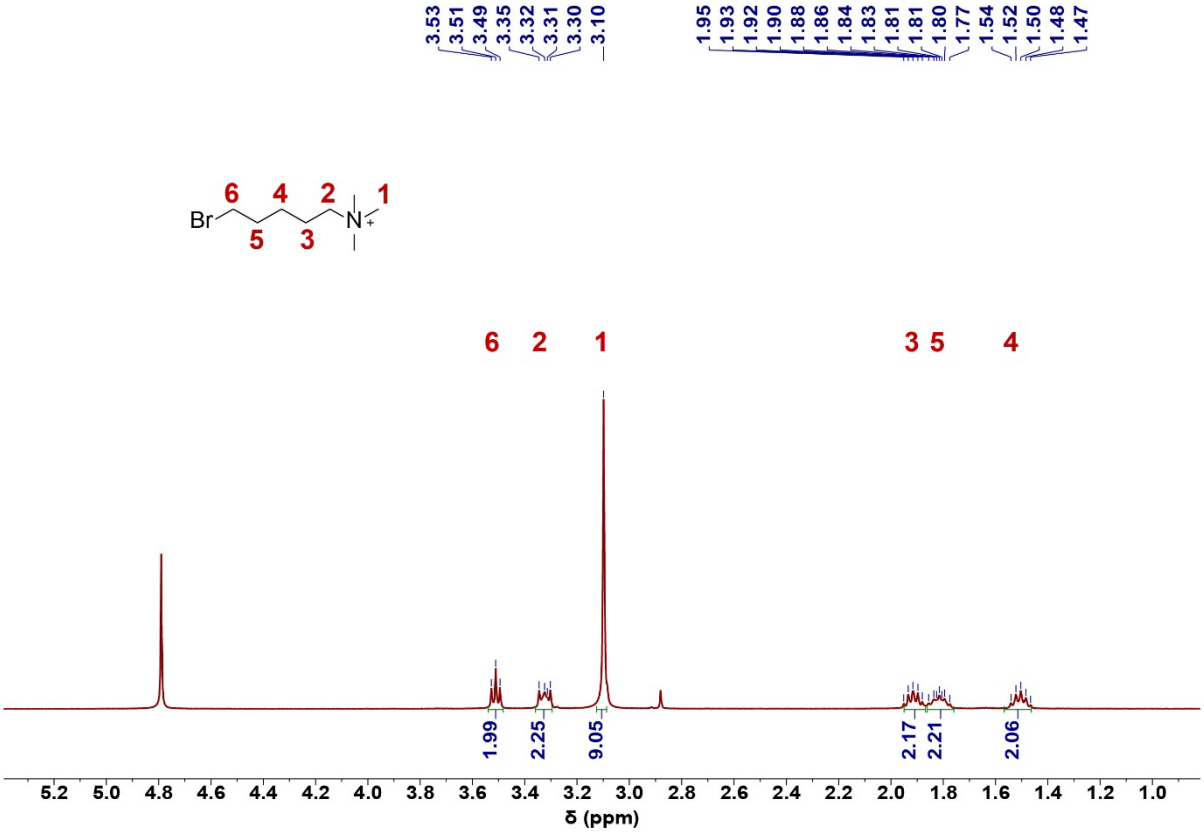

Figure S14 ^{1}H NMR spectrum of M_3, recorded in D_2O at 25 °C.

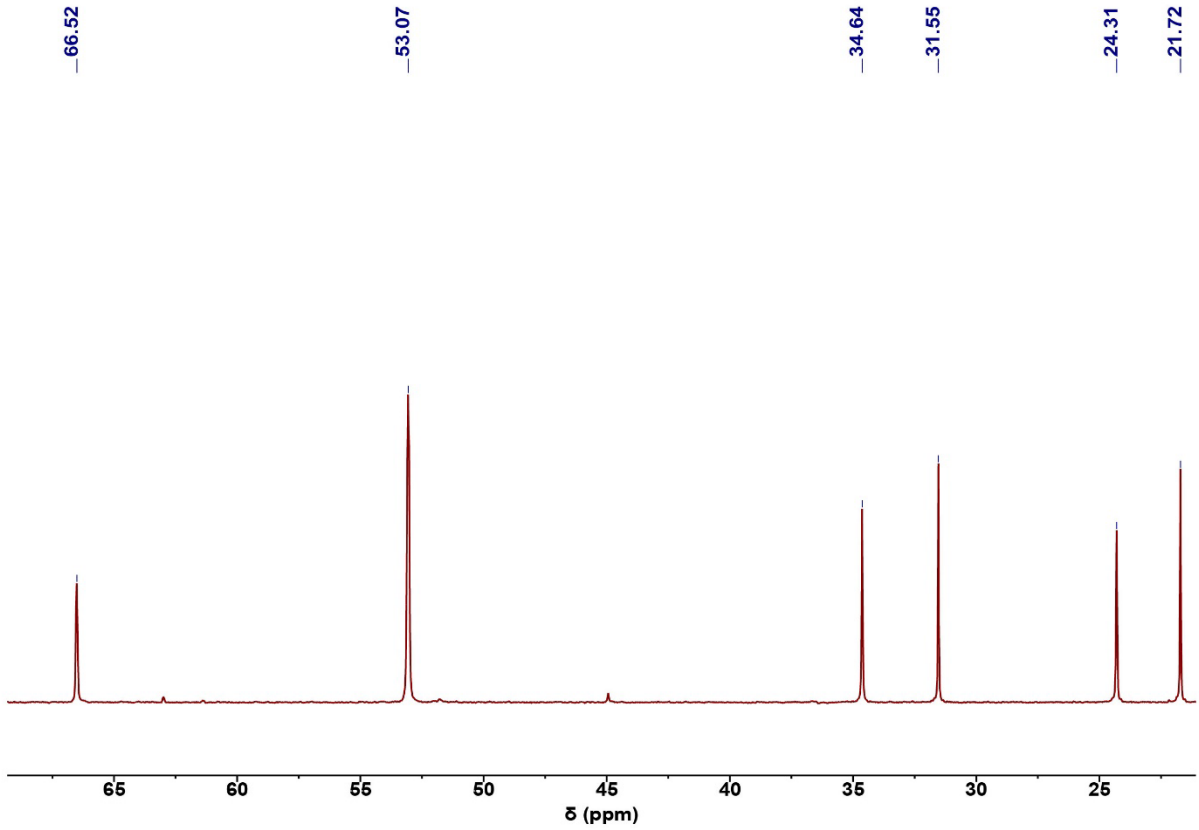

Figure S15 ^{13}C NMR spectrum of M_3, recorded in D_2O at 25 °C.

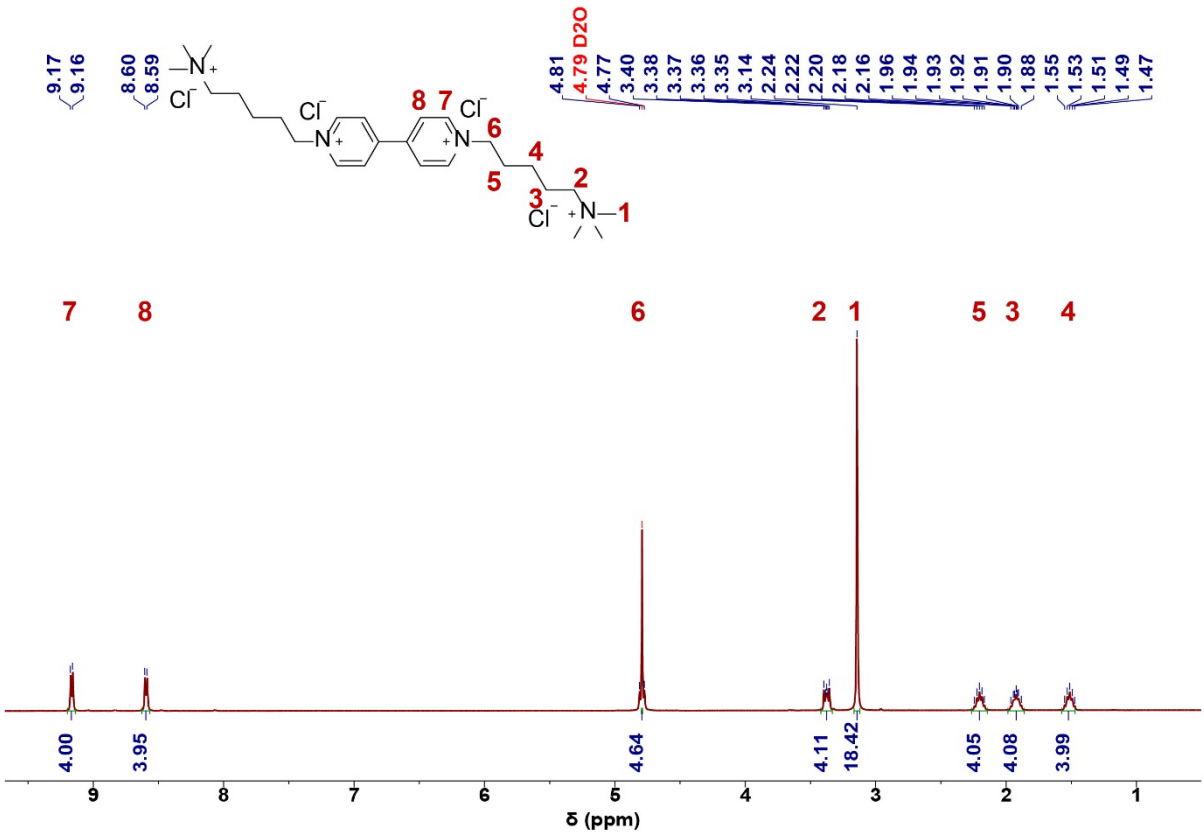

Figure S16 ^{1}H NMR spectrum of TMAPE-V-Cl, recorded in D_2O at 25 °C.

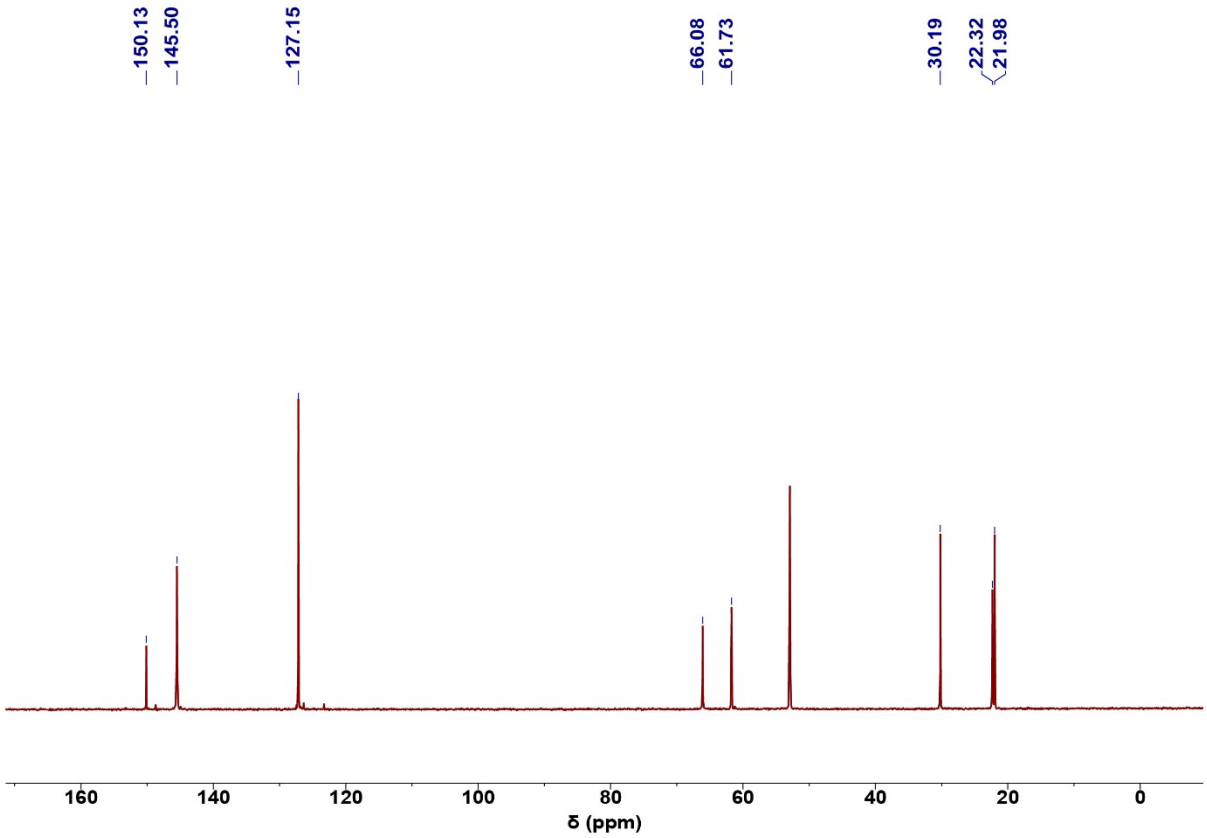

Figure S17 ^{13}C NMR spectrum of TMAPE-V-Cl, recorded in D_2O at 25 °C.

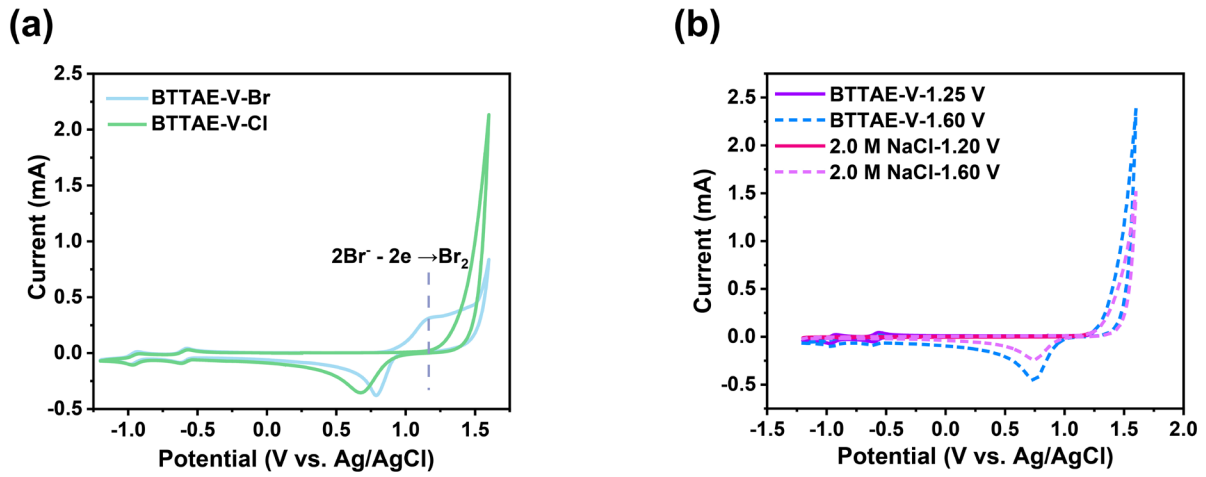

Figure S18 (a) CV comparison of 4.0 mM BTTAE-V-Br (blue trace) and BTTAE-V-Cl (green trace) in 2.0 M NaCl supporting electrolyte. The dashed line indicates the onset of the bromide oxidation reaction ($2Br^-$ - 2e → Br_2). (b) CV curves of 4.0 mM BTTAE-V-Cl in 2.0 M NaCl and the pure 2.0 M NaCl supporting electrolyte recorded at different anodic potential limits (up to +1.20 V, +1.25 V and +1.60 V vs. Ag/AgCl). All measurements were performed at a scan rate of 100 mV s^{-1} using a glassy carbon working electrode.

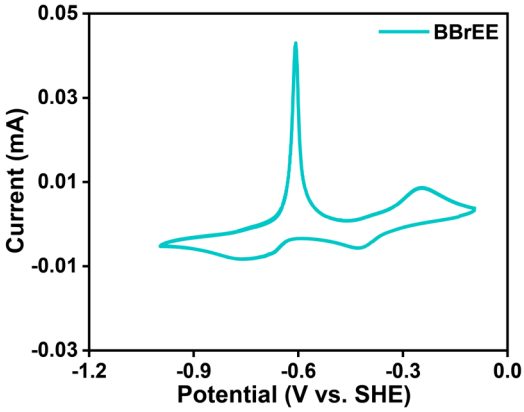

Figure S19 CV of BBrEE. The electroactive species were tested at a concentration of 2.0 mM in 1.0 M NaCl electrolyte at a scan rate of 100 mV s^{-1} using a glassy carbon working electrode.

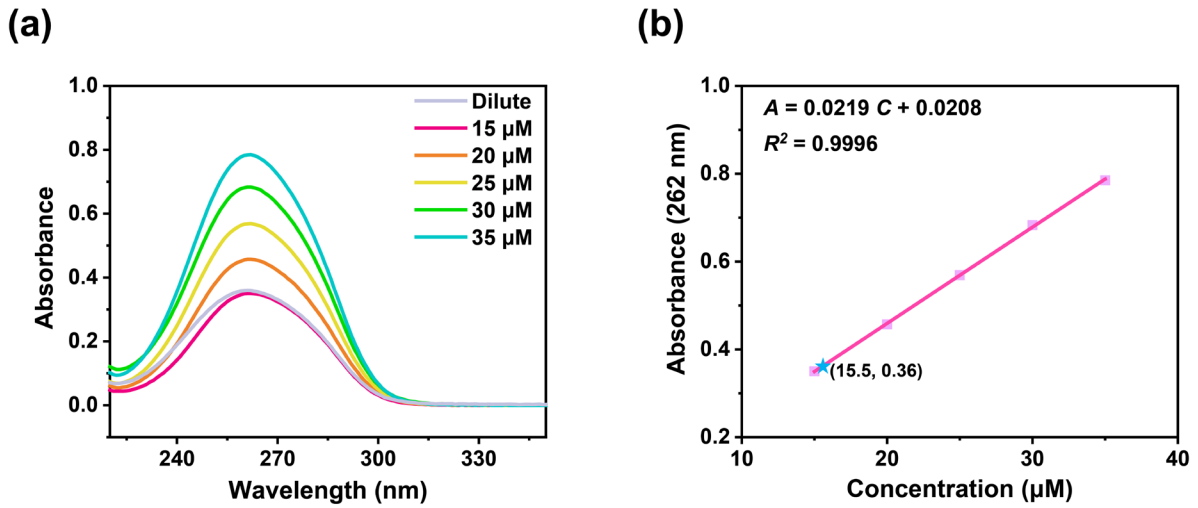

Figure S20 (a) UV-vis absorption spectra of BTTAE-V-Cl in deionized water (without added NaCl) at concentrations ranging from 15 to 35 μM, recorded over the wavelength range of 220–350 nm. The grey trace corresponds to a 10^5-diluted saturated BTTAE-V-Cl solution and is included for comparison to indicate the spectral features at the solubility limit. (b) Corresponding calibration curve showing the linear relationship between absorbance and concentration at the characteristic wavelength (λ_{max} = 262 nm), with a coefficient of determination of R^2 = 0.9996.

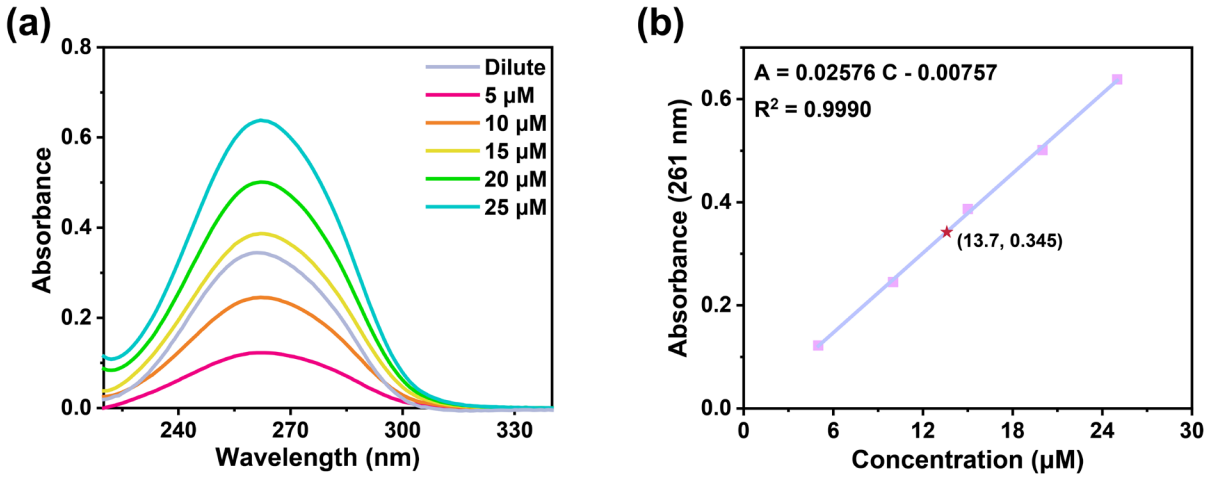

Figure S21 (a) UV-vis absorption spectra of BTTAE-V-Cl in 2.0 M NaCl aqueous solution at different concentrations ranging from 5 μM to 25 μM (220–350 nm). The grey trace represents the absorption spectrum of a 10^5 diluted saturated BTTAE-V-Cl solution. (b) Corresponding calibration curve showing the linear relationship between absorbance and concentration at the characteristic wavelength (λ_{max} = 261 nm), with a coefficient of determination of R^2 = 0.9990.

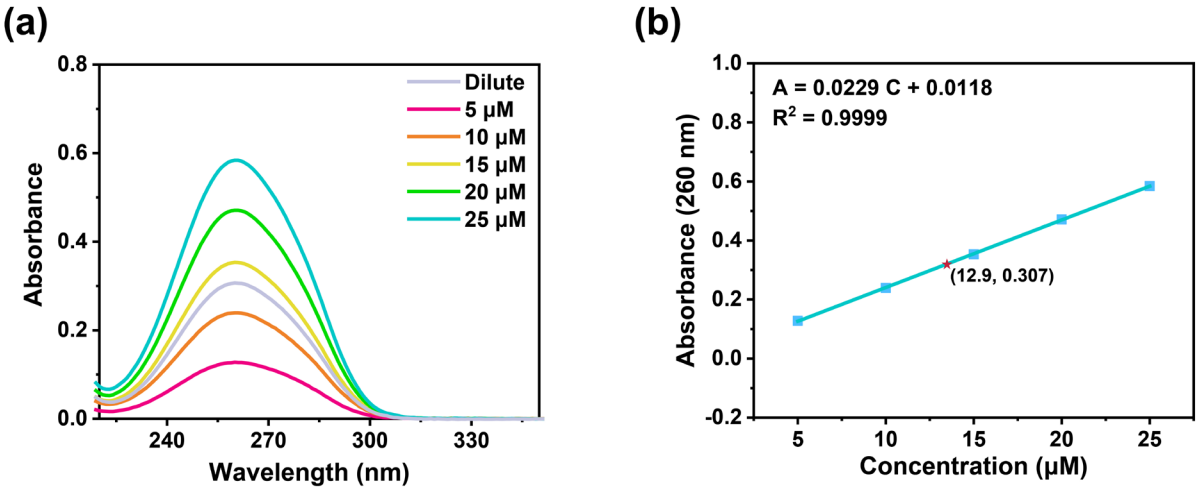

Figure S22 (a) UV-vis absorption spectra of TMAPE-V-Cl in deionized water (without added NaCl) at concentrations ranging from 5 to 25 μM, recorded over the wavelength range of 220–350 nm. The grey trace corresponds to a 10^5-diluted saturated TMAPE-V-Cl solution and is included for comparison to indicate the spectral features at the solubility limit. (b) Corresponding calibration curve showing the linear relationship between absorbance and concentration at the characteristic wavelength (λ_{max} = 260 nm), with a coefficient of determination of R^2=0.9999.

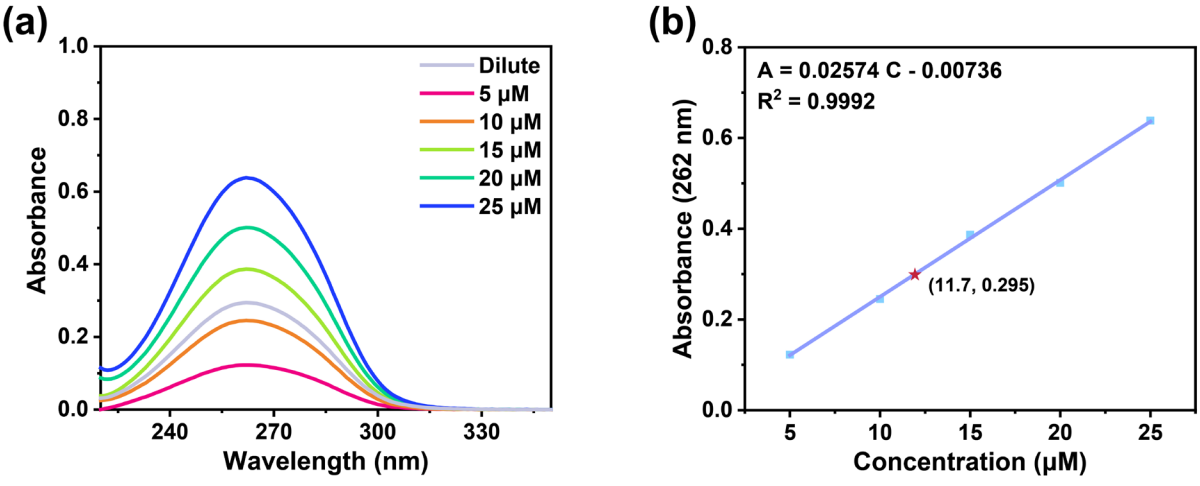

Figure S23 (a) UV-vis absorption spectra of TMAPE-V-Cl in 2.0 M NaCl aqueous solution at different concentrations ranging from 5 μM to 25 μM (220–350 nm). The grey trace represents the absorption spectrum of a 10^5 diluted saturated TMAPE-V-Cl solution. (b) Corresponding calibration curve showing the linear relationship between absorbance and concentration at the characteristic wavelength (λ_{max} = 262 nm), with a coefficient of determination of R^2 = 0.9992.

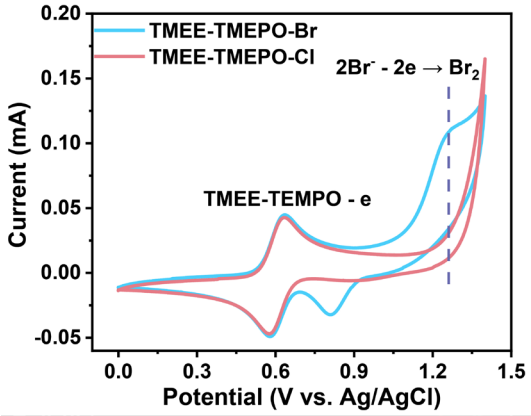

Figure S24 CV of TMEE-TEMPO-Br (blue trace) and TMEE-TEMPO-Cl (red trace). The electroactive species were tested at a concentration of 4.0 mM in 2.0 M NaCl electrolyte at a scan rate of 100 mV s^{-1} using a glassy carbon working electrode.

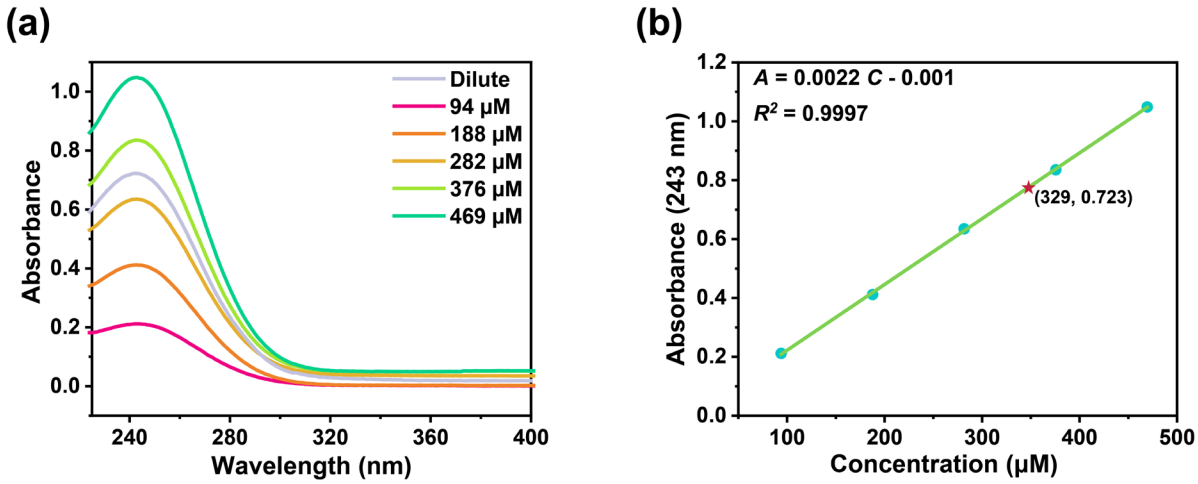

Figure S25 (a) UV-vis absorption spectra of TMEE-TEMPO-Cl in deionized water (without added NaCl) at concentrations ranging from 94 to 469 μM, recorded over the wavelength range of 220–400 nm. The grey trace corresponds to a 2.5×10^5 diluted saturated TMEE-TEMPO-Cl solution and is included for comparison to indicate the spectral features at the solubility limit. (b) Corresponding calibration curve showing the linear relationship between absorbance and concentration at the characteristic wavelength (λ_{max} = 243 nm), with a coefficient of determination of $R^2 = 0.9997$.

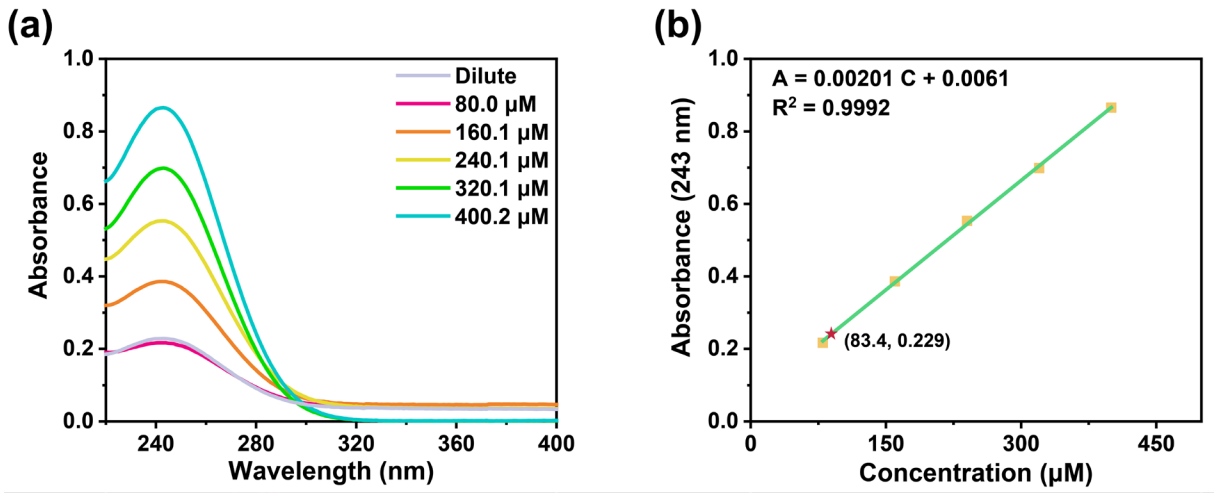

Figure S26 (a) UV-vis absorption spectra of TMEE-TEMPO-Cl in 2.0 M NaCl aqueous solution at different concentrations ranging from 80 μM to 400.2 μM (220–400 nm). The grey trace represents the absorption spectrum of a 2.5×10^5 diluted saturated TMEE-TEMPO-Cl solution. (b) Corresponding calibration curve showing the linear relationship between absorbance and concentration at the characteristic wavelength (λ_{max} = 243 nm), with a coefficient of determination of $R^2 = 0.9992$.

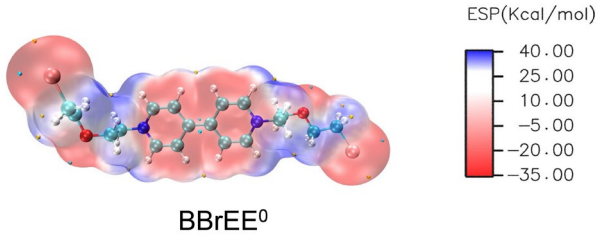

Figure S27 Molecular electrostatic potential (ESP) distribution of the two-electron-reduced reference molecule BBrEE0 mapped on the electron density surface. Red and blue regions represent relatively negative and positive electrostatic potentials, respectively. The electrostatic potential ranges are -33.5 to 37.8 kcal mol^{-1}.

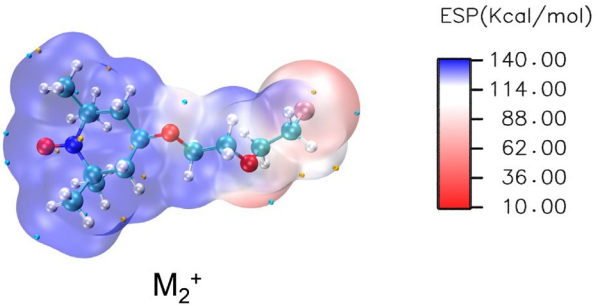

Fig. S28 Molecular electrostatic potential (ESP) distribution of the oxidized reference molecule M_2^+ mapped on the electron density surface. Red and blue regions represent relatively negative and positive electrostatic potentials, respectively. The electrostatic potential ranges are 12.2 to 138.8 kcal mol^{-1}.

Optimized coordinates of $BTTAE^{2+}$ (two-electron reduced state)

Atom	X (Å)	Y (Å)	Z (Å)

C	-8.834349	-1.559735	0.349423
N	-7.490464	-1.776601	-0.284320
C	-7.340382	-3.237849	-0.603145
C	-7.402947	-0.992140	-1.561069
C	-6.373133	-1.405445	0.662968
C	-6.358684	0.048802	1.109642
O	-5.239918	0.149740	1.983908
C	-5.110878	1.451750	2.556378
C	-3.832749	1.505909	3.374064
N	-2.615109	1.414604	2.575165
C	-2.174339	2.523842	1.863592
C	-1.215042	2.445119	0.914764
C	-0.590235	1.180176	0.542422
C	0.418849	1.071884	-0.396860
C	0.983811	2.212902	-1.109762
C	1.967111	2.077289	-2.026050
N	2.486512	0.838214	-2.394440
C	3.795731	0.782163	-3.038840
C	4.949304	1.129077	-2.100347
O	4.976386	0.307304	-0.929159
C	5.508848	-1.000895	-1.109728
C	7.024643	-1.076409	-1.193995
N	7.798176	-0.617451	0.031175
C	7.760037	0.878106	0.170006
C	7.268369	-1.249326	1.283434
C	9.227675	-1.038468	-0.155413
C	2.026695	-0.270517	-1.690428
C	1.044252	-0.194565	-0.766528
C	-1.140379	0.039269	1.268920
C	-2.101143	0.177471	2.209493
H	-9.591987	-1.952793	-0.325262
H	-8.858540	-2.092119	1.297826
H	-8.994359	-0.496146	0.502884
H	-7.437739	-3.804453	0.320506

H	-8.123472	-3.516485	-1.304552
H	-6.359320	-3.396027	-1.045989
H	-6.406445	-1.122946	-1.977995
H	-8.154290	-1.377752	-2.246910
H	-7.595934	0.056608	-1.353237
H	-6.479120	-2.057116	1.529521
H	-5.442845	-1.643702	0.148464
H	-6.231277	0.733227	0.264838
H	-7.274055	0.318765	1.645512
H	-5.086452	2.205195	1.759032
H	-5.970365	1.661348	3.205376
H	-3.815374	2.449389	3.923824
H	-3.823754	0.694643	4.104439
H	-2.638040	3.462400	2.137775
H	-0.916619	3.368768	0.437579
H	0.621044	3.214543	-0.921169
H	2.389105	2.926424	-2.547927
H	3.919177	-0.217296	-3.457476
H	3.812230	1.489493	-3.872000
H	5.893931	1.066613	-2.650847
H	4.837515	2.151126	-1.734334
H	5.135184	-1.457673	-2.031880
H	5.131154	-1.598159	-0.280908
H	7.294154	-2.121669	-1.347638
H	7.414570	-0.493724	-2.027366
H	6.734007	1.191165	0.328865
H	8.382204	1.151432	1.020043
H	8.154792	1.319347	-0.742699
H	7.945262	-1.000377	2.098140
H	6.278886	-0.853312	1.494547
H	7.229625	-2.327174	1.140260
H	9.594204	-0.614920	-1.088270
H	9.268945	-2.125058	-0.189767
H	9.807584	-0.661776	0.684358

H	2.496467	-1.208741	-1.954273
H	0.732480	-1.119959	-0.301505
H	-0.781615	-0.962588	1.075547
H	-2.507566	-0.668088	2.747394

Optimized coordinates of $BBrEE^{0}$ (Two-electron reduced state)

Atom	X (Å)	Y (Å)	Z (Å)
C	-7.980029	1.384590	0.630923
C	-7.671434	-0.076911	0.352172
O	-6.868284	-0.596234	1.416222
C	-5.457751	-0.430296	1.221874
C	-4.873091	-1.599651	0.427544
N	-3.448733	-1.416913	0.168110
C	-2.527148	-1.686265	1.176196
C	-1.254206	-1.234829	1.137411
C	-0.758430	-0.391879	0.053516
C	0.548778	0.051267	-0.034808
C	1.040745	0.900380	-1.115400
C	2.310986	1.359853	-1.150751
N	3.233191	1.085719	-0.146410
C	4.652259	1.326984	-0.381654
C	5.294667	0.201168	-1.195816
O	6.675982	0.468753	-1.456201
C	7.545975	0.073591	-0.392017
C	8.892595	0.693384	-0.697788
Br	10.201695	0.181044	0.696439
C	2.840607	0.200609	0.852088
C	1.583416	-0.287436	0.937303
C	-1.791385	-0.053281	-0.920261
C	-3.050160	-0.535165	-0.833246
H	-7.082982	1.996226	0.680373
H	-8.574958	1.508511	1.531905
H	-7.162538	-0.192366	-0.608334
H	-8.589450	-0.665508	0.331057

H	-5.007011	-0.388232	2.215160
H	-5.246327	0.515042	0.711970
H	-5.008582	-2.529922	0.981714
H	-5.386450	-1.701402	-0.530441
H	-2.896403	-2.306154	1.982948
H	-0.603849	-1.524810	1.951640
H	0.389508	1.191665	-1.928313
H	2.676523	1.987406	-1.953144
H	5.146128	1.433766	0.585456
H	4.758203	2.270900	-0.919136
H	4.805902	0.124359	-2.169027
H	5.185099	-0.758481	-0.678352
H	7.613784	-1.019240	-0.355826
H	7.170412	0.432520	0.570431
H	9.303098	0.337956	-1.639428
H	8.850491	1.779265	-0.686830
H	3.608343	-0.052028	1.571668
H	1.366040	-0.946348	1.767041
H	-1.571278	0.600424	-1.753368
H	-3.816539	-0.281629	-1.554045

Optimized coordinates of TMEE-TEMPO^{2+} (One-electron oxidized state)

Atom	X (Å)	Y (Å)	Z (Å)
C	-4.111323	-0.532343	-0.533137
C	-5.092472	-0.678834	-1.690692
C	-2.748024	-0.019852	-1.019257
C	-1.848519	0.511708	0.082741
O	-0.655873	0.990129	-0.553356
C	0.500016	1.017450	0.291909
C	1.224409	-0.325061	0.260379
O	2.397599	-0.274535	1.084527
C	3.566704	0.207946	0.417409
C	4.302718	-1.000804	-0.157713
N	5.507205	-0.675270	-1.014691

C	6.148210	-1.974245	-1.410543
C	6.504449	0.143503	-0.248144
C	5.103109	0.058613	-2.260783
C	-2.545011	1.658359	0.807730
C	-3.874676	1.270304	1.466782
C	-4.678063	2.502658	1.864525
C	-3.691065	0.344467	2.689722
N	-4.708826	0.479088	0.452345
O	-5.884868	0.625309	0.458871
H	-4.952337	-2.115806	0.715375
H	-3.772139	-2.625677	-0.507698
H	-3.209664	-1.861317	0.983894
H	-5.308060	0.287865	-2.148701
H	-6.023223	-1.148754	-1.375318
H	-4.614996	-1.318465	-2.434052
H	-2.909870	0.776773	-1.750178
H	-2.267634	-0.855122	-1.531600
H	-1.586933	-0.286461	0.780719
H	1.147041	1.806565	-0.095636
H	0.228494	1.273875	1.320136
H	0.591283	-1.113882	0.670076
H	1.482458	-0.591161	-0.769412
H	4.168710	0.716709	1.169643
H	3.298166	0.928244	-0.357116
H	4.665577	-1.630513	0.653587
H	3.631570	-1.583903	-0.787738
H	7.004576	-1.754953	-2.044841
H	5.416472	-2.570024	-1.952003
H	6.466954	-2.491624	-0.508017
H	6.742348	-0.378345	0.676629
H	6.079701	1.121665	-0.038519
H	7.395895	0.251263	-0.862153
H	4.350692	-0.532316	-2.778928
H	5.987928	0.177287	-2.882417

H	4.706437	1.034127	-1.993322
H	-2.725388	2.461418	0.088542
H	-1.914611	2.055816	1.605104
H	-4.034265	3.108517	2.503661
H	-4.956476	3.093627	0.990591
H	-5.573419	2.239115	2.426492
H	-3.254493	0.968870	3.471049
H	-4.654323	-0.031071	3.036023
H	-3.019503	-0.487166	2.496549

Optimized coordinates of M_2^+ (One-electron oxidized state)

Atom	X (Å)	Y (Å)	Z (Å)
C	-2.700665	-2.810443	-0.896795
C	-1.917818	-1.527672	-1.149611
C	-1.315533	-1.552097	-2.571571
C	-0.867458	-1.289117	-0.057189
C	-0.294290	0.125145	-0.035856
O	0.629123	0.274603	1.046814
C	1.935732	-0.226823	0.756872
C	2.760030	-0.129061	2.030287
O	4.086826	-0.611919	1.785226
C	5.011946	0.394813	1.363880
C	5.695099	0.968462	2.592779
Br	6.976056	2.387923	2.057931
C	-1.414858	1.123120	0.199163
C	-2.518197	1.090623	-0.868428
C	-3.764144	1.833032	-0.400914
C	-2.052179	1.655766	-2.228550
N	-2.917089	-0.366141	-1.130026
O	-4.054025	-0.600508	-1.368581
H	-1.971972	-3.618056	-0.815640
H	-3.380644	-3.037907	-1.717090
H	-3.261933	-2.751480	0.037215
H	-0.755269	-2.486080	-2.639764

H	-0.634010	-0.727780	-2.761842
H	-2.105642	-1.559878	-3.323175
H	-1.319293	-1.491650	0.917386
H	-0.084145	-2.029488	-0.225456
H	0.229338	0.346611	-0.970305
H	1.890124	-1.271524	0.433176
H	2.389907	0.365957	-0.046079
H	2.328424	-0.761733	2.807779
H	2.784730	0.901381	2.396946
H	4.501176	1.176814	0.796159
H	5.737510	-0.091293	0.710391
H	6.281737	0.217809	3.115885
H	4.989961	1.442436	3.271014
H	-1.022859	2.141547	0.207574
H	-1.862484	0.924570	1.176653
H	-4.209159	1.351908	0.471472
H	-3.448540	2.838810	-0.120627
H	-4.507806	1.912233	-1.193149
H	-1.083447	1.274663	-2.538601
H	-1.971324	2.734960	-2.088528
H	-2.792938	1.457467	-3.003497

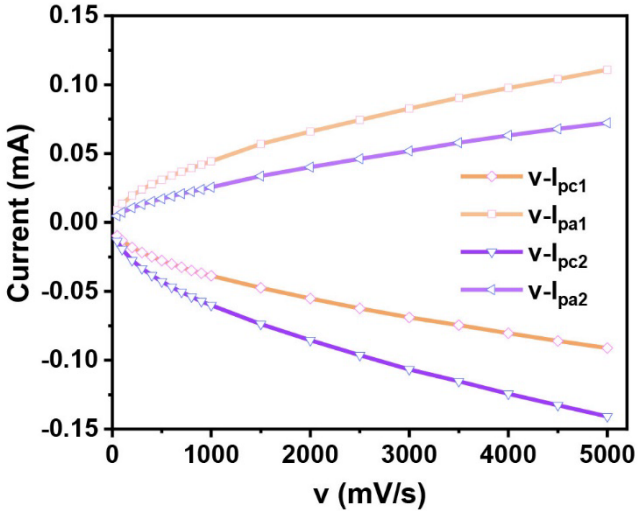

Figure S29 Plot of peak current (i_p) as a function of scan rate (v) for 1 mM BTTAE-V-Cl in 1 M NaCl aqueous solution. The orange curves represent the anodic (i_{pa1}) and cathodic (i_{pc1}) peak currents of the first redox couple as a function of scan rate, while the purple curves correspond to the anodic (i_{pa2}) and cathodic (i_{pc2}) peak currents of

the second redox couple. Electrochemical measurements were conducted using a glassy carbon working electrode, a platinum wire counter electrode, and an Ag/AgCl (saturated KCl) reference electrode.

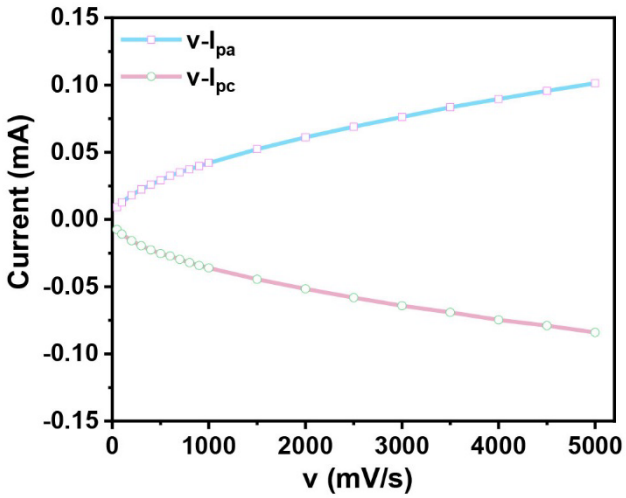

Figure S30 Plot of peak current (i_p) versus scan rate (v) for 1 mM TMEE-TEMPO-Cl in 1 M NaCl aqueous solution. The blue curve represents the anodic peak current (i_{pa}) as a function of scan rate, while the red curve represents the cathodic peak current (i_{pc}). Electrochemical measurements were performed using a glassy carbon working electrode, a platinum wire counter electrode, and an Ag/AgCl (saturated KCl) reference electrode.

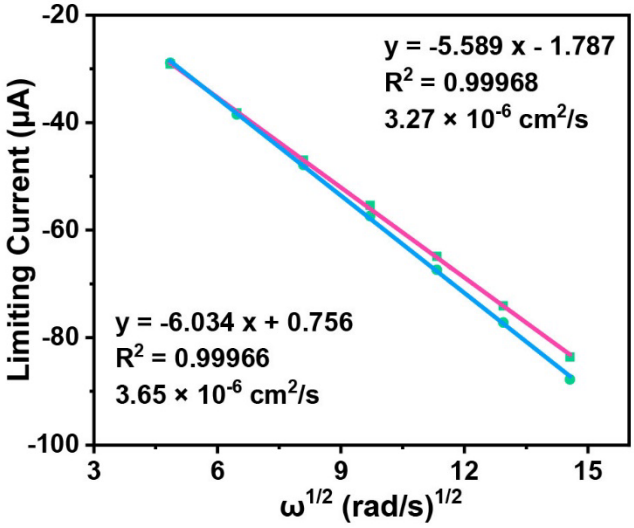

Figure S31 Levich plots of BTTAE-V-Cl obtained from rotating disk electrode (RDE) experiments. The plots show the linear relationship between the limiting current (i_{lim}) and the square root of the rotation rate ($\omega^{1/2}$) for the first electron transfer step (red line) and the second electron transfer step (blue line, with the contribution from the first step subtracted). Both Levich lines exhibit excellent linearity, and the corresponding diffusion coefficients (D) for each redox step were calculated from the slopes using the Levich equation. The coefficients of determination (R^2) for the first and second electron transfer steps are 0.99968 and 0.99966, respectively.

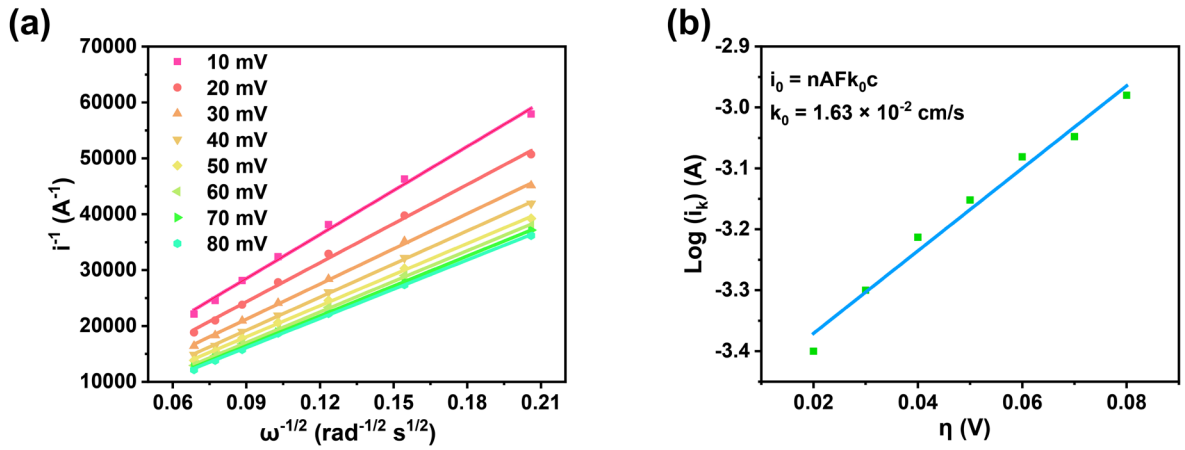

Figure S32 RDE analysis of the first electron-transfer process of BTTAE-V-Cl. (a) Koutecký–Levich (K–L) plots: linear relationships between the reciprocal limiting current ($1/i$) and the reciprocal square root of the rotation rate ($\omega^{-1/2}$) at different applied potentials. The good linearity of the K–L plots indicates first-order reaction kinetics and enables extraction of the kinetic current (i_k). (b) Tafel plot: logarithm of the kinetic current ($log\ i_k$), obtained from RDE analysis, plotted as a function of the overpotential (η). Linear fitting of the Tafel region provides the heterogeneous electron-transfer rate constant for the system.

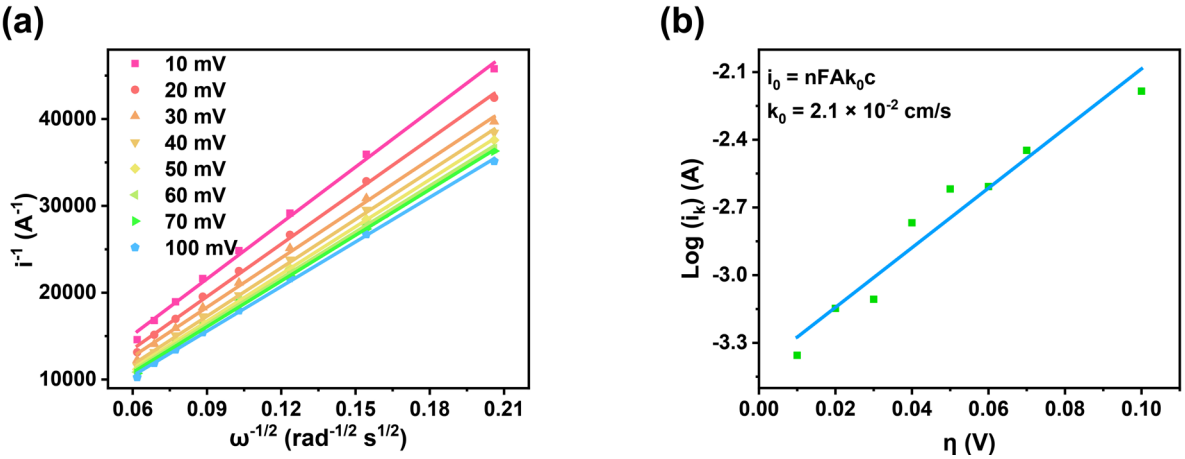

Figure S33 RDE analysis of the second electron-transfer process of BTTAE-V-Cl (after subtraction of the limiting current from the first electron-transfer step). (a) Koutecký–Levich (K–L) plots showing the linear relationships between the reciprocal limiting current ($1/i$) and the reciprocal square root of the rotation rate ($\omega^{-1/2}$) at different applied potentials. The excellent linearity of the K–L plots indicates first-order reaction kinetics and enables the determination of the kinetic current (i_k). (b) Tafel plots constructed from the kinetic current (i_k) extracted from RDE analysis, in which $\log(i_k)$ is plotted as a function of overpotential (η). Linear fitting of the Tafel region provides the heterogeneous electron-transfer rate constant for the second electron-transfer process.

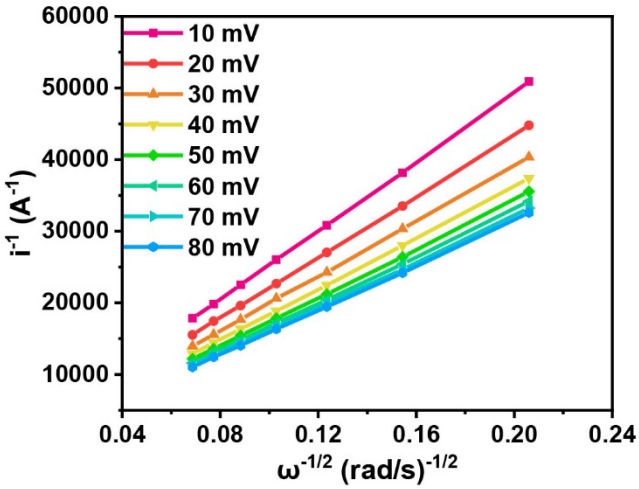

Figure S34 RDE analysis of the electron transfer process of TMEE-TEMPO-Cl. Koutecký–Levich (K–L) plots showing the linear relationship between the reciprocal of the limiting current ($1/i$) and the reciprocal square root of the rotation rate ($\omega^{-1/2}$) at different applied potentials. The good linearity of the K–L lines indicates that the electron transfer process follows first-order reaction kinetics, and the kinetic current (i_k) was calculated accordingly using the Koutecký–Levich equation.

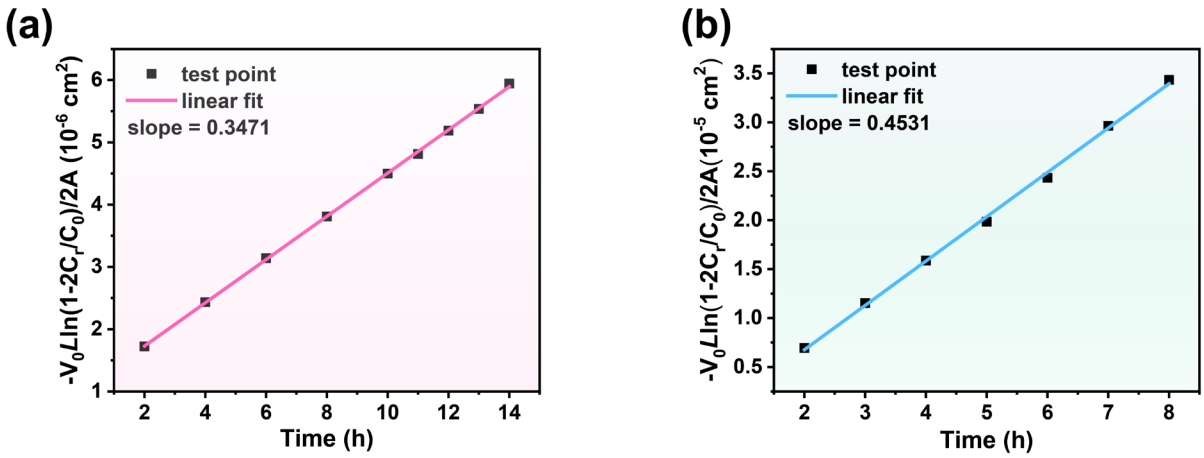

Figure S35 Determination of permeability coefficients for the active species across a Selemion DSV anion-exchange membrane using a two-compartment diffusion cell. (a) Linear relationship between $-V_0L\ln(1-2C_t/C_0)/2A$ and time for BTTAE-V-Cl. (b) Linear relationship between $-V_0L\ln(1-2C_t/C_0)/2A$ and time for TMEE-TEMPO-Cl. The permeability coefficients obtained from the slopes of the linear fits are 9.64×10^{-11} cm^2 s^{-1} for BTTAE-V-Cl and 1.26×10^{-9} cm^2 s^{-1} for TMEE-TEMPO-Cl, respectively.

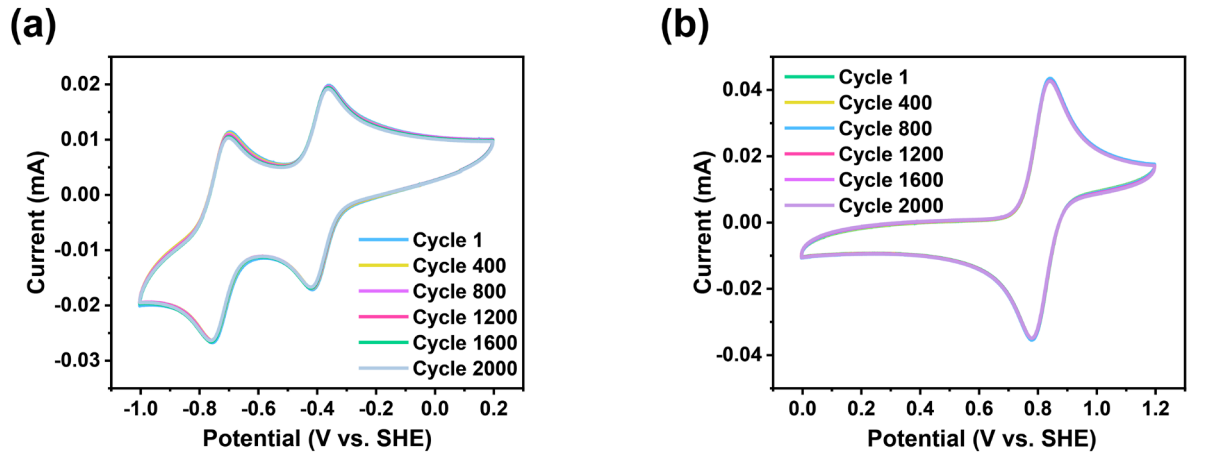

Figure S36 (a) CV of BTTAE-V-Cl recorded at a concentration of 1.0 mM in 1.0 M NaCl aqueous electrolyte using a glassy carbon working electrode at a scan rate of 100 mV s^{-1}. (b) CV of TMEE-TEMPO-Cl recorded at a concentration of 2.0 mM under identical conditions.

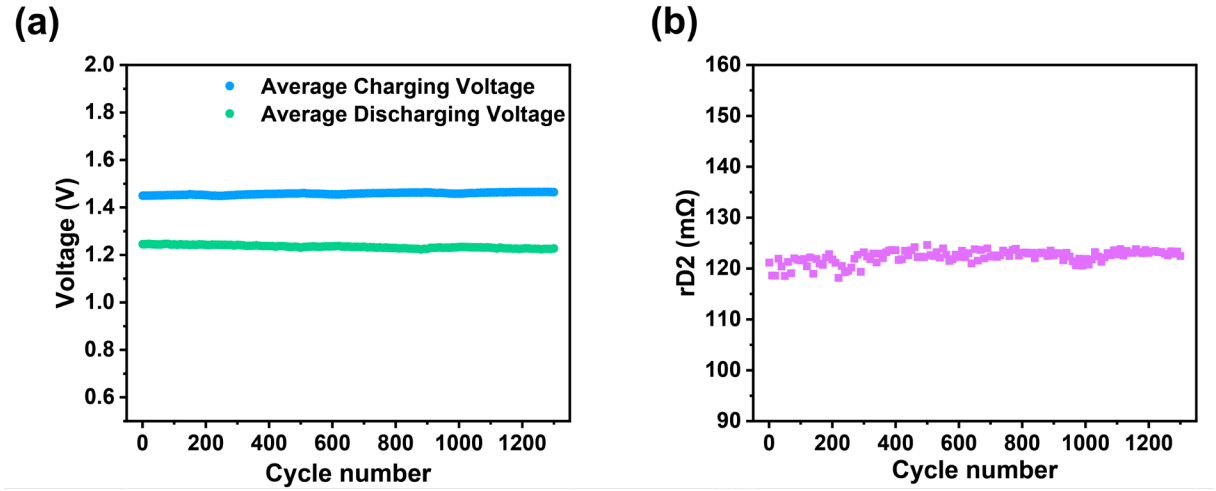

Figure S37 (a) Average charge voltage (blue trace) and average discharge voltage (green trace) during 1300 galvanostatic charge–discharge cycles at a current density of 40 mA cm^{-2}. (b) Evolution of the parameter r_D2, extracted from the voltage profiles during cycling, as a function of cycle number.

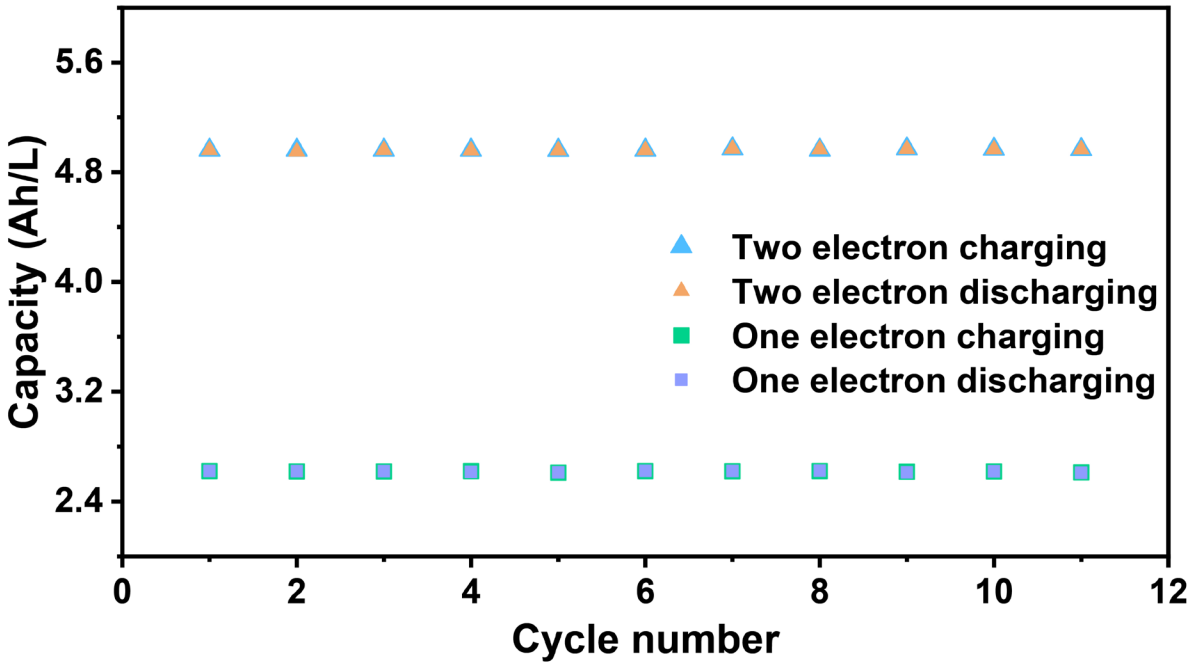

Figure S38 Comparison of the cycling performance of the BTTAE-V-Cl/TMEE-TEMPO-Cl flow battery operated in single-electron and two-electron modes. The two-electron mode is represented by light-blue triangles (charge) and orange triangles (discharge), while the single-electron mode is represented by green squares (charge) and light-blue squares (discharge).

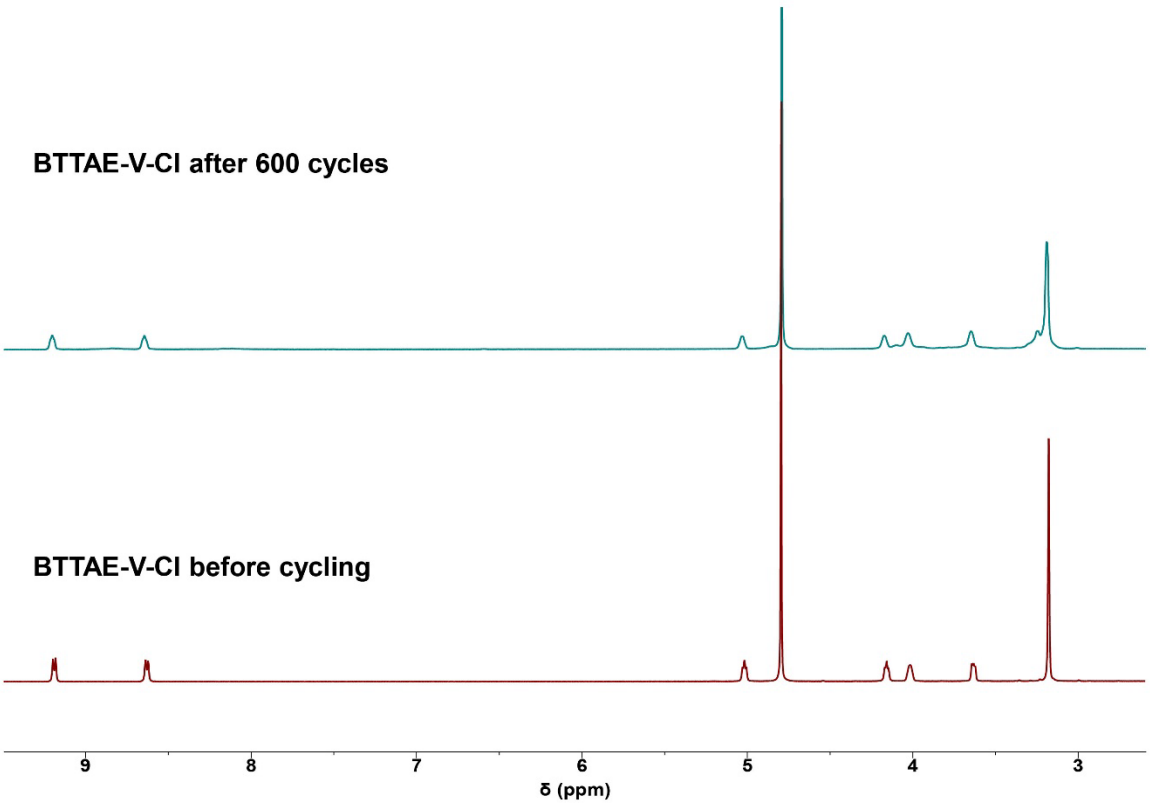

Figure S39 Comparison of the ^{1}H NMR spectra of BTTAE-V-Cl before and after 600 cycles, recorded in D_2O at 25 °C.

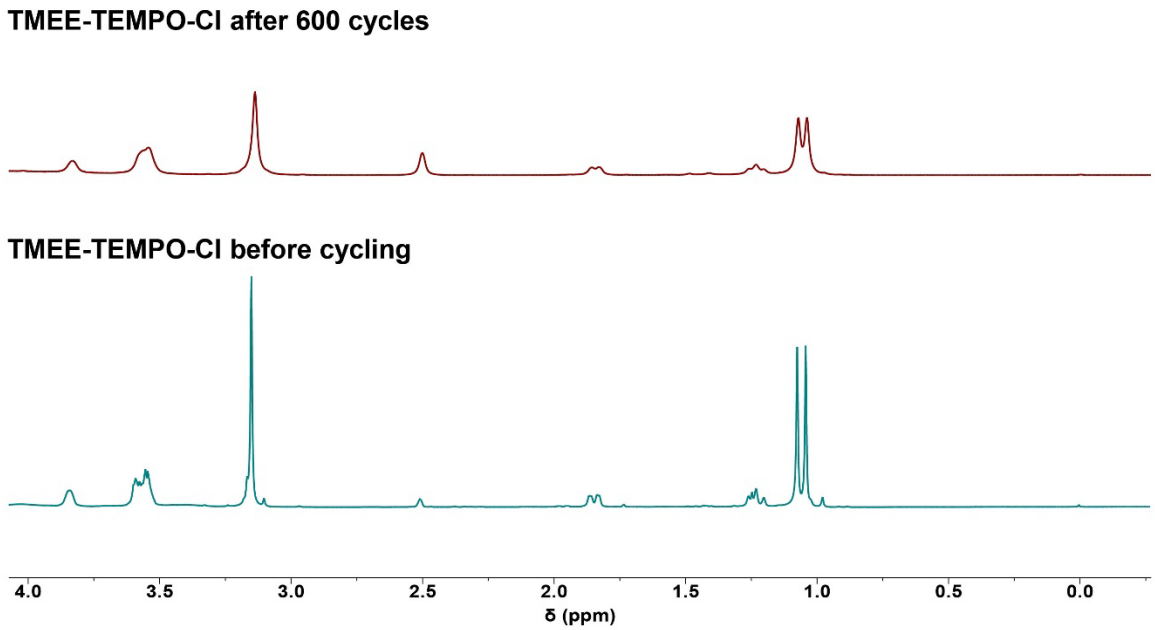

Figure S40 Comparison of the 1H NMR spectra of TMEE-TEMPO-Cl before and after 600 cycles, recorded in DMSO-d_6 at 25 °C.

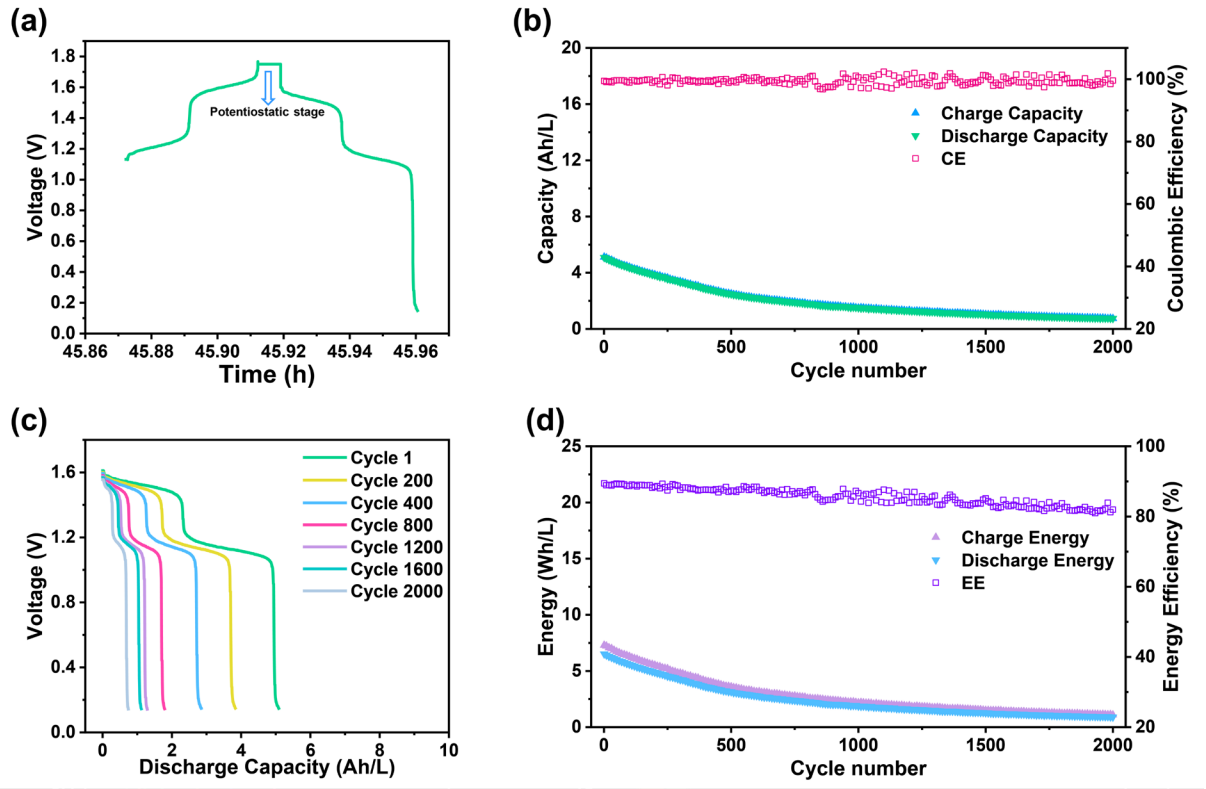

Figure S41 Long-term galvanostatic–potentiostatic (GP) cycling performance of the 0.1 M BTTAE-V-Cl / 0.2 M TMEE-TEMPO-Cl flow battery. (a) Representative voltage profile within a single charge–discharge cycle, highlighting the potentiostatic charging stage at 1.75 V (applied after galvanostatic charging at 20 mA cm^{-2} until the cutoff voltage, followed by a constant-voltage step until the current decays to 1 mA cm^{-2}). (b) Charge-discharge capacity and CE and (d) Charge-discharge energy and EE as a function of cycle number during 2000 cycles. (c) Discharge voltage–capacity profiles at selected cycle numbers (1, 200, 400, 800, 1200, 1600, and 2000),

illustrating the progressive change in accessible capacity and voltage polarization during cycling. All measurements were conducted at a current density of 20 mA cm^{-2} with a cutoff voltage of 0.15–1.75 V. The GP protocol enables enhanced capacity utilization but also introduces extended high-voltage residence time, providing insight into the origin of capacity decay under these operating conditions.

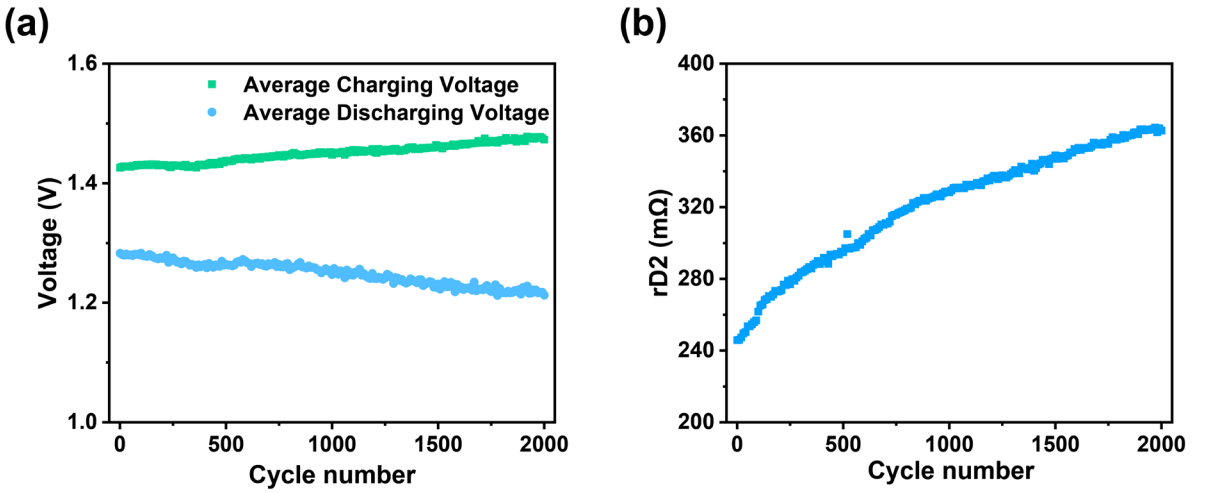

Figure S42 Evolution of voltage polarization and interfacial resistance during long-term GP cycling. (a) Average charge and discharge voltages as a function of cycle number. (b) Evolution of the parameter r_D2, extracted from the voltage profiles during cycling, as a function of cycle number. The gradual increase in charge voltage, decrease in discharge voltage, and the continuous rise in r_D2 collectively indicate progressively enhanced polarization and increased resistance during cycling.

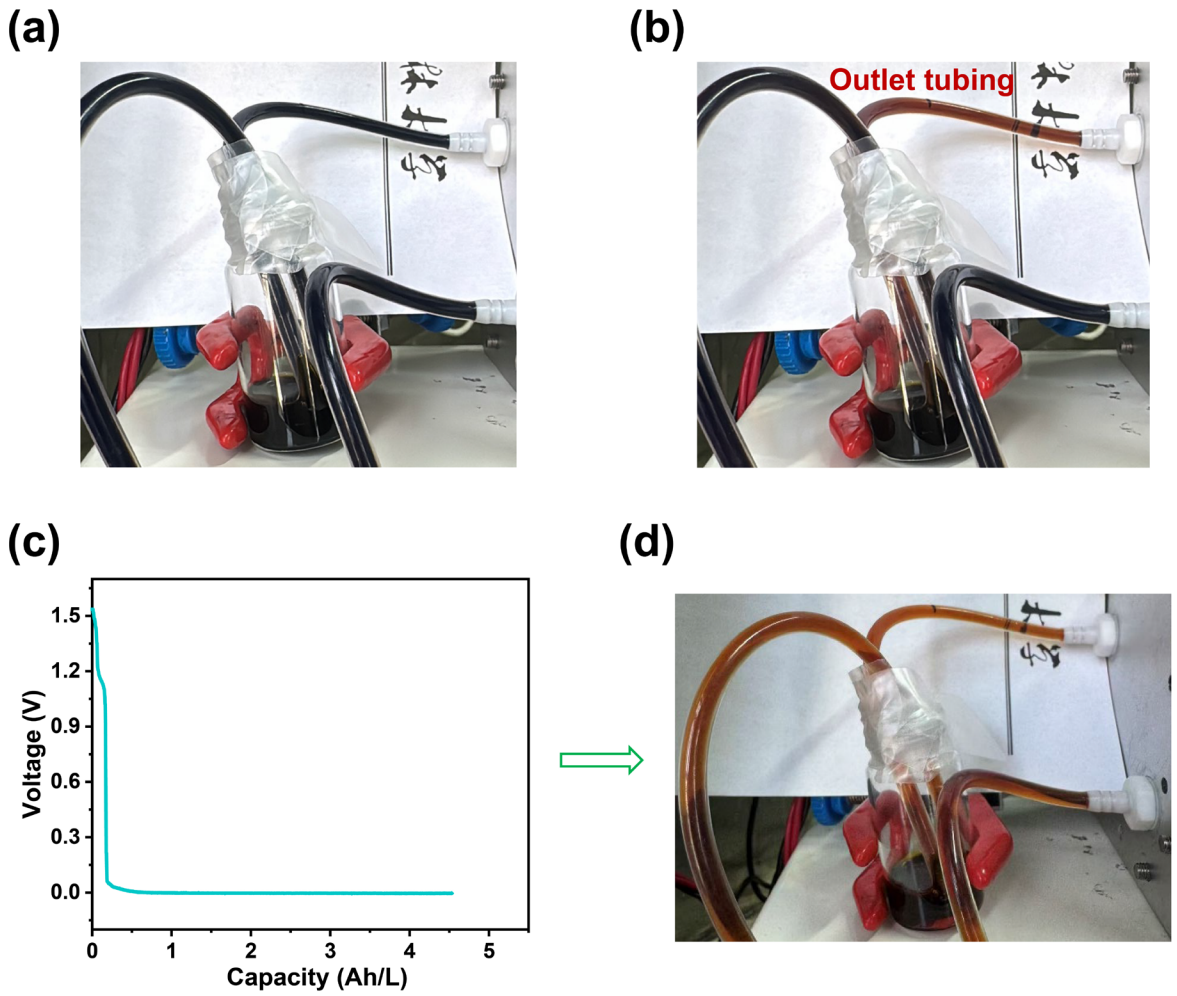

Figure S43 Visual evidence of spatial SOC heterogeneity and recoverable capacity during discharge. (a) Photograph of the electrolyte during discharge at the second plateau, where most of the electrolyte in the reservoir and tubing remains in the colored (charged) state. (b) At the discharge cutoff, only the electrolyte in the outlet tubing returns to its initial color, while the bulk electrolyte remains colored. (c) Discharge voltage–capacity profile when the cutoff voltage is extended to 0 V, showing the emergence of an additional discharge plateau. (d) Corresponding photograph after extended discharge, where the anolyte returns to its initial color.

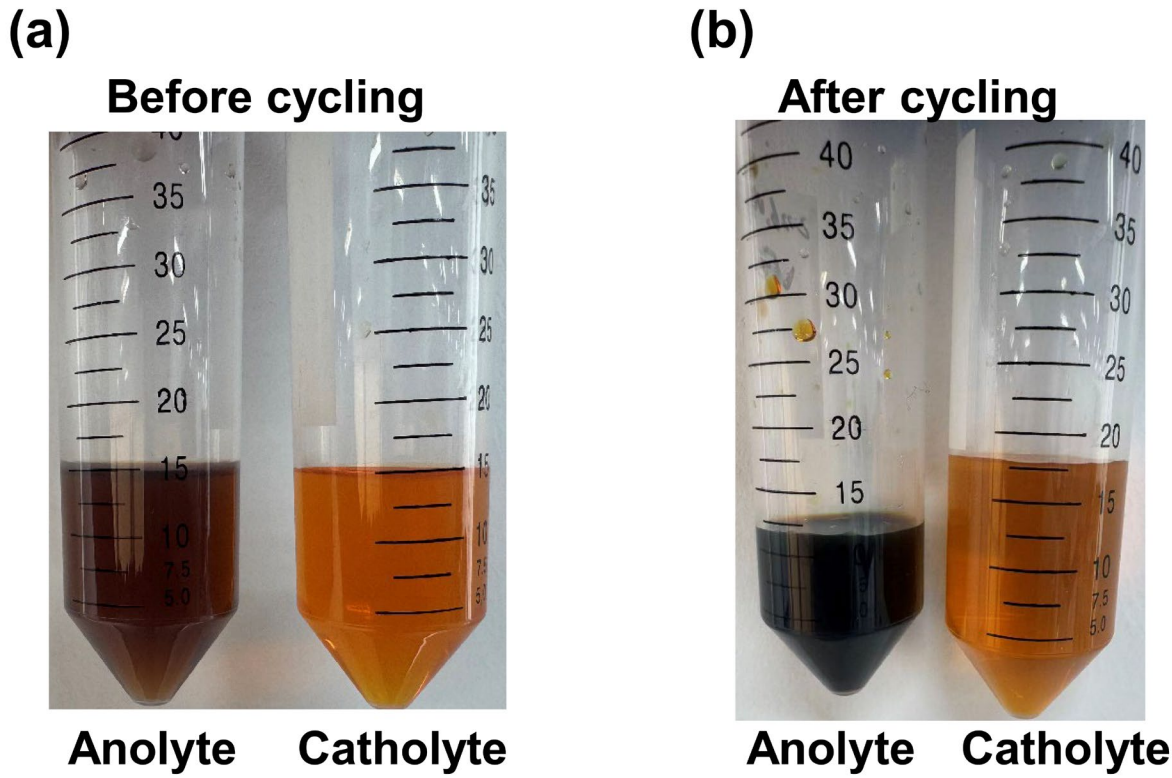

Figure S44 Photographs of the anolyte and catholyte reservoirs before (a) and after (b) cycling. The initial electrolyte compositions were 0.1 M BTTAE-V-Cl in 2.0 M NaCl (15 mL) as the anolyte and 0.2 M TMEE-TEMPO-Cl in 2.0 M NaCl (15 mL) as the catholyte. The flow battery was operated under galvanostatic charge–discharge conditions at a current density of 40 mA cm^{-2} within a voltage window of 0.15–1.75 V using a DSV separator.

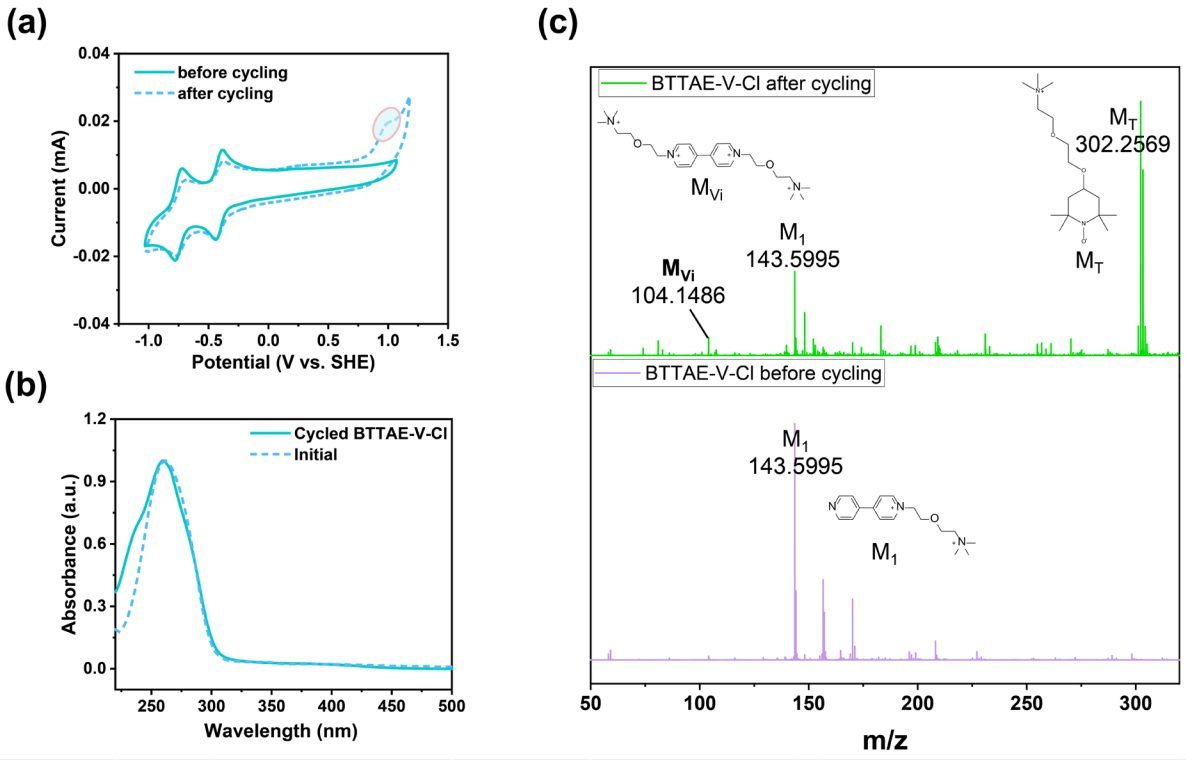

Figure S45 Electrochemical and spectroscopic characterization of the anolyte before and after cycling. (a) Cyclic voltammograms of BTTAE-V-Cl before and after flow battery operation (scan rate: 100 mV s^{-1}). An additional oxidation feature appears near +1 V in the cycled anolyte. (b) UV–vis absorption spectra of the anolyte before and after cycling, showing noticeable changes in the spectral profile after operation. (c) LC–MS spectra of the anolyte before and after cycling, where a signal at m/z = 302.2569 is observed in the cycled sample.

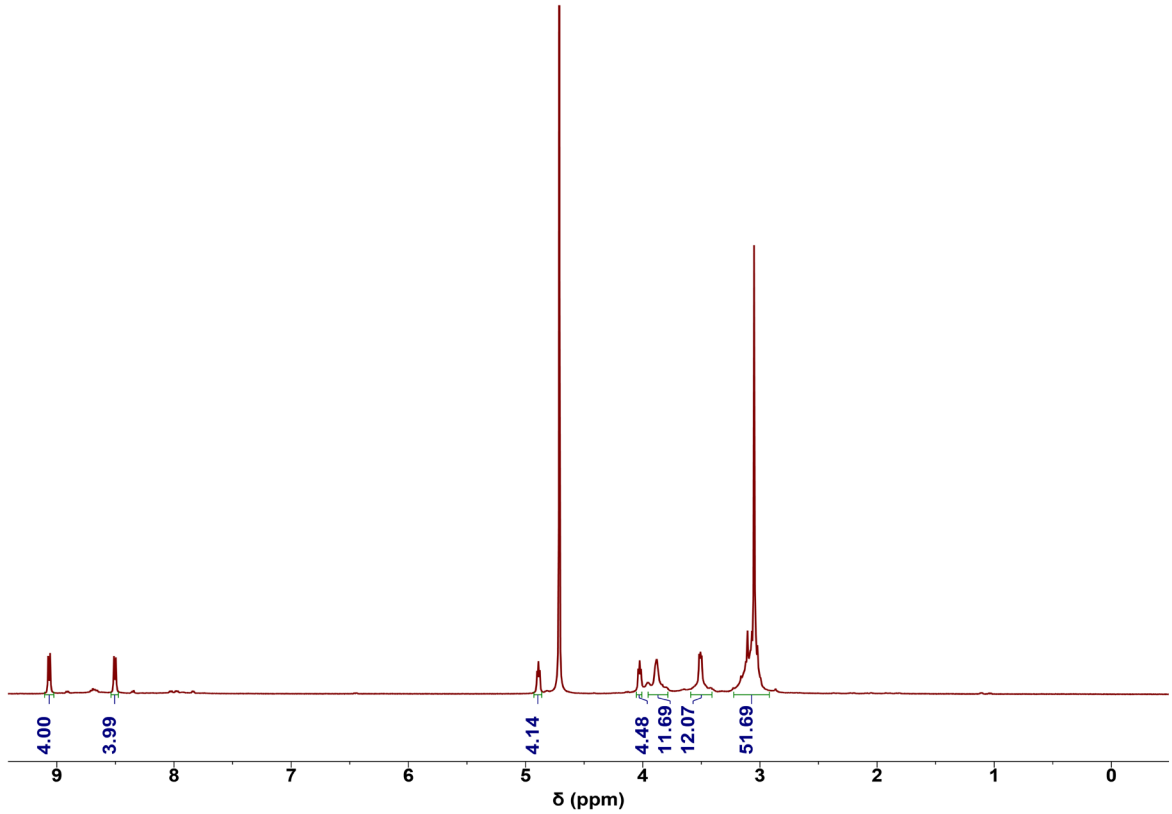

Figure S46 ^{1}H NMR spectrum (400 MHz, D_2O) of 0.1 M BTTAE-V-Cl collected from the anolyte reservoir after cycling.

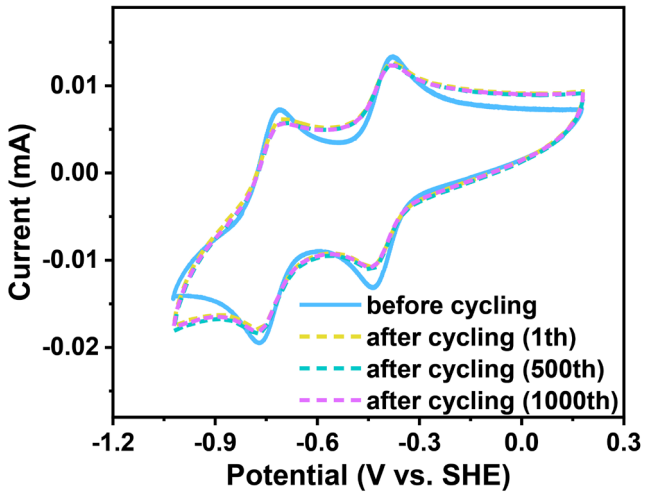

Figure S47 Cyclic voltammetry of BTTAE-V-Cl before and after flow battery operation. CV curves were recorded at a scan rate of 100 mV s^{-1}. The blue line represents the pristine electrolyte, while the dashed lines correspond to

the cycled electrolyte at different scan numbers: the 1st cycle (yellow), 500th cycle (green), and 1000th cycle (pink).

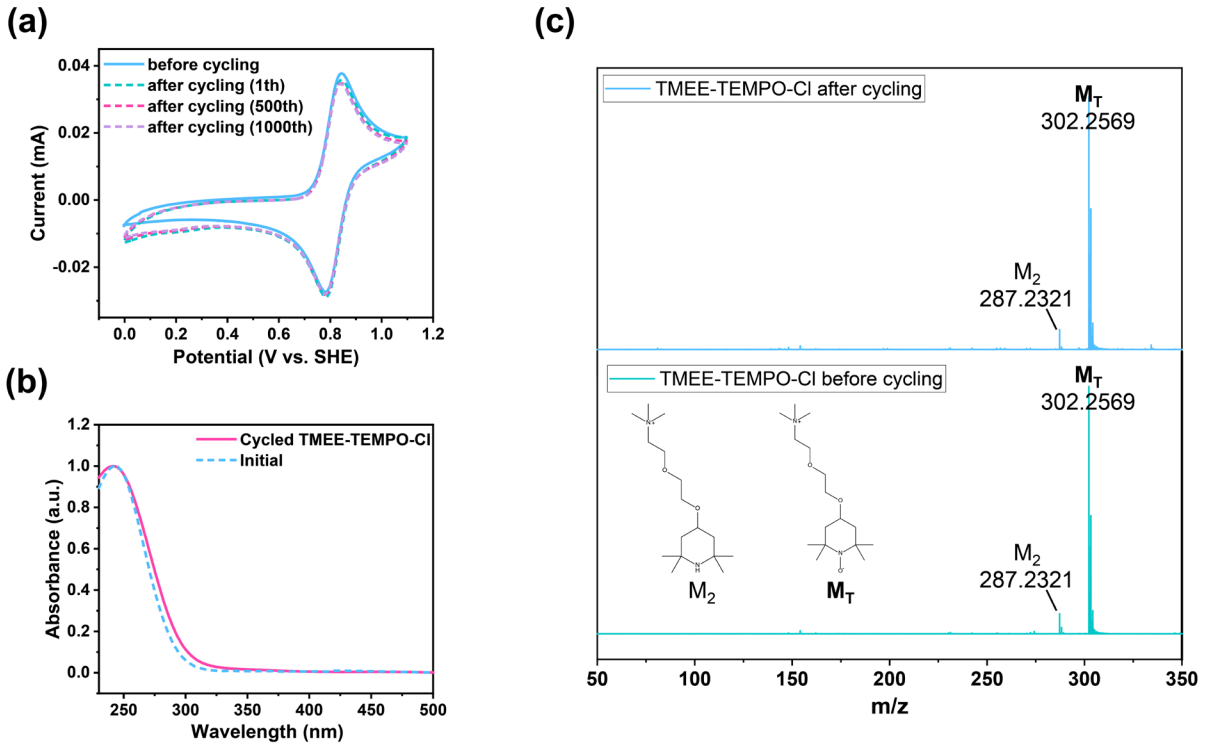

Figure S48 Electrochemical and spectroscopic characterization of TMEE-TEMPO-Cl before and after flow battery operation. (a) Cyclic voltammograms recorded at a scan rate of 100 mV s^{-1}. The blue line represents the pristine electrolyte, while the dashed lines correspond to the cycled electrolyte at different scan numbers: the 1st cycle (green), 500th cycle (pink), and 1000th cycle (purple). (b) UV–vis absorption spectra of TMEE-TEMPO-Cl before and after cycling. (c) LC–MS spectra of the electrolyte before and after cycling.

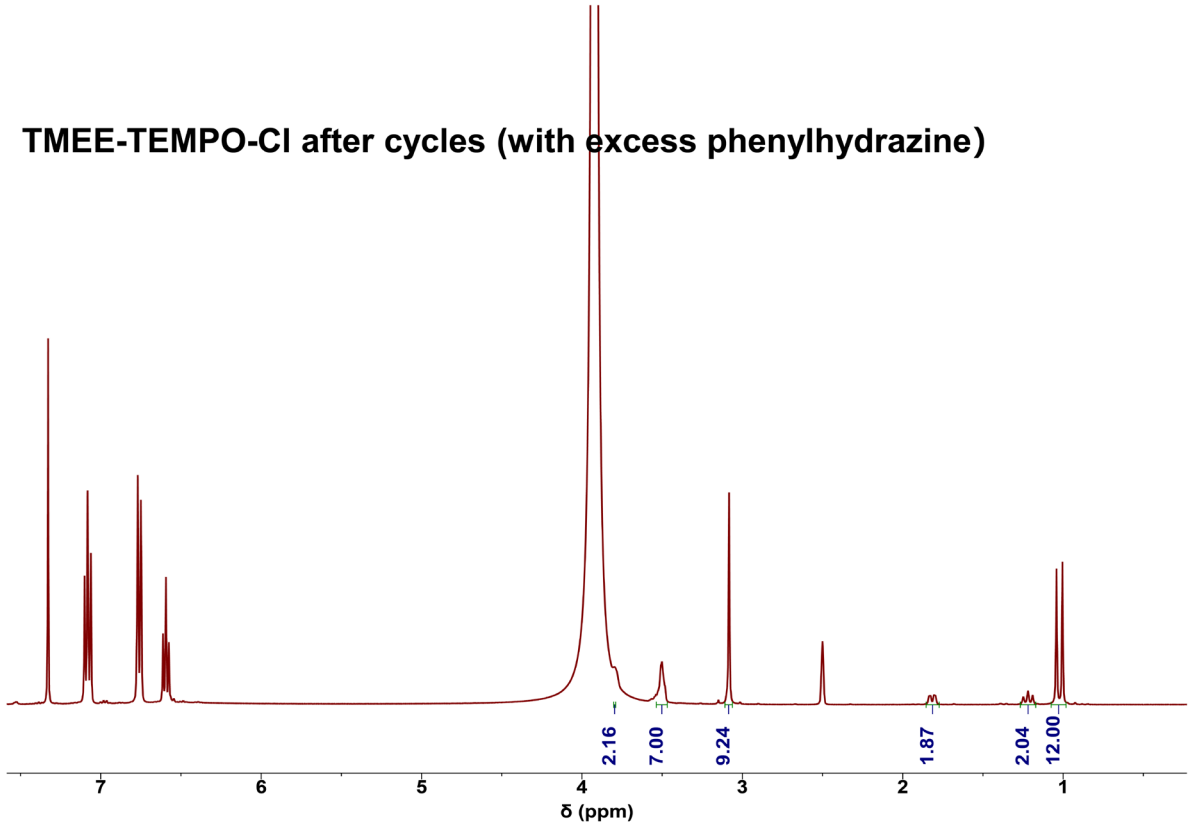

Figure S49 ^{1}H NMR spectrum (400 MHz, DMSO-d_6) of 0.2 M TMEE-TEMPO-Cl collected from the catholyte reservoir after flow battery cycling, recorded in the presence of excess phenylhydrazine as a reducing agent.

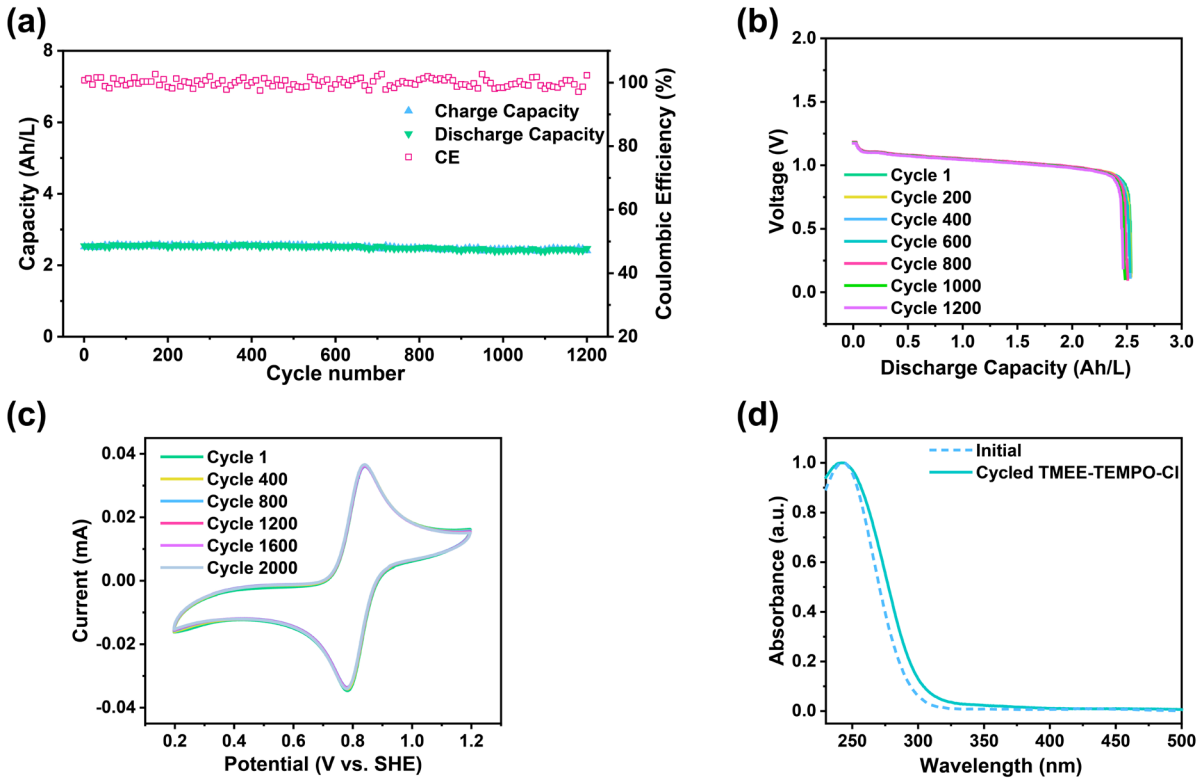

Figure S50 Electrochemical performance and post-cycling characterization of the asymmetric cell with TMEE-TEMPO-Cl as the capacity-limiting side. The cell was assembled using 0.3 M BTTAE-V-Cl (30 mL) as the anolyte

and 0.1 M TMEE-TEMPO-Cl (15 mL) as the catholyte and cycled at 40 mA cm^{-2} within a voltage window of 0.1–1.8 V. (a) Charge capacity, discharge capacity, and coulombic efficiency as a function of cycle number. (b) Discharge voltage profiles at selected cycles (1, 200, 400, 600, 800, 1000, and 1200). (c) Cyclic voltammograms of the cycled catholyte recorded at different scan numbers (1, 400, 800, 1200, 1600, and 2000 cycles) at a scan rate of 100 mV s^{-1}. (d) UV–vis absorption spectra of TMEE-TEMPO-Cl before and after cycling.

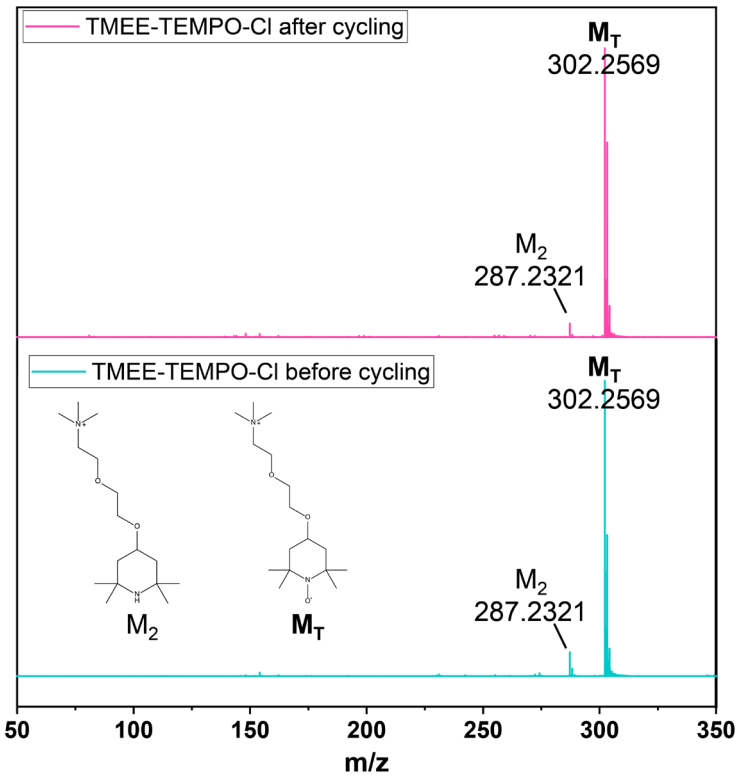

Figure S51 Comparison of LC–MS spectra of TMEE-TEMPO-Cl catholyte before and after cycling in an asymmetric cell with TMEE-TEMPO-Cl as the capacity-limiting side.

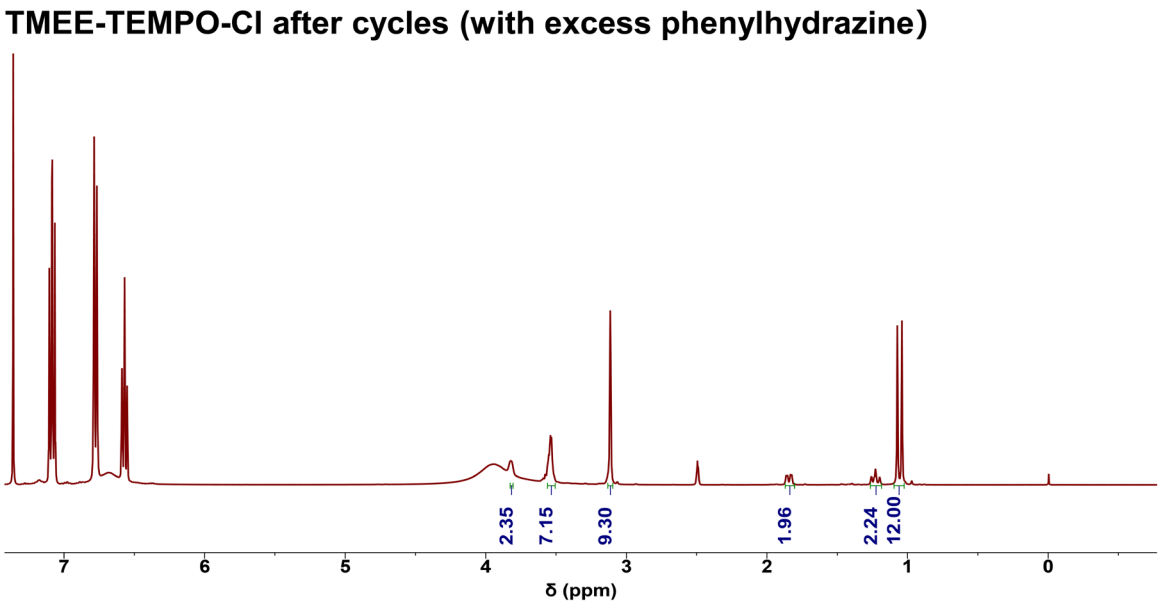

Figure S52 ^{1}H NMR spectrum (400 MHz, DMSO-d_6) of 0.1 M TMEE-TEMPO-Cl collected from the catholyte reservoir after flow battery cycling, recorded in the presence of excess phenylhydrazine as a reducing agent.

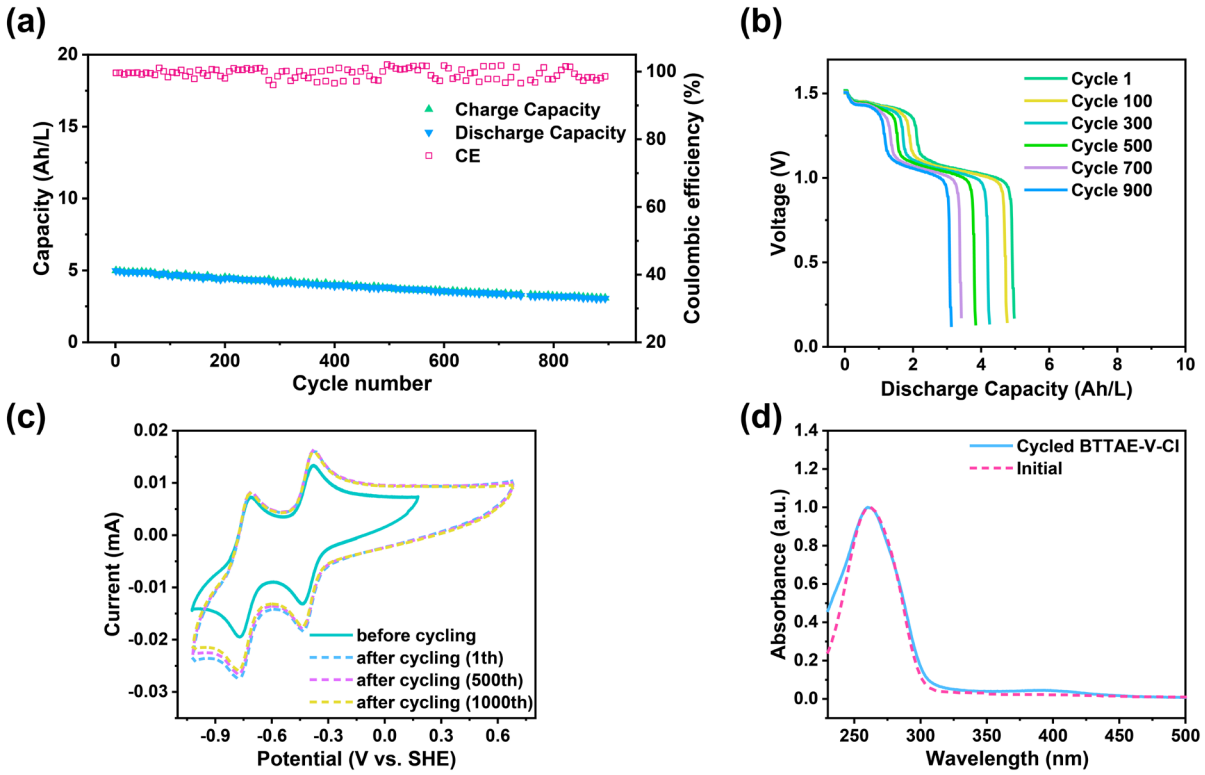

Figure S53 Electrochemical performance and post-cycling characterization of the asymmetric cell with BTTAE-V-Cl as the capacity-limiting component. The cell was configured with 0.1 M BTTAE-V-Cl (15 mL) as the anolyte and 0.4 M TMEE-TEMPO-Cl (30 mL) as the catholyte, operated at 40 mA cm^{-2} within a voltage window of 0.15–1.8 V. (a) Charge/discharge capacity and coulombic efficiency as a function of cycle number. (b) Charge–discharge voltage profiles at selected cycles. (c) Cyclic voltammograms of the anolyte before cycling and after selected cycles at a scan rate of 100 mV s^{-1}. (d) UV–vis absorption spectra of the anolyte before and after cycling.

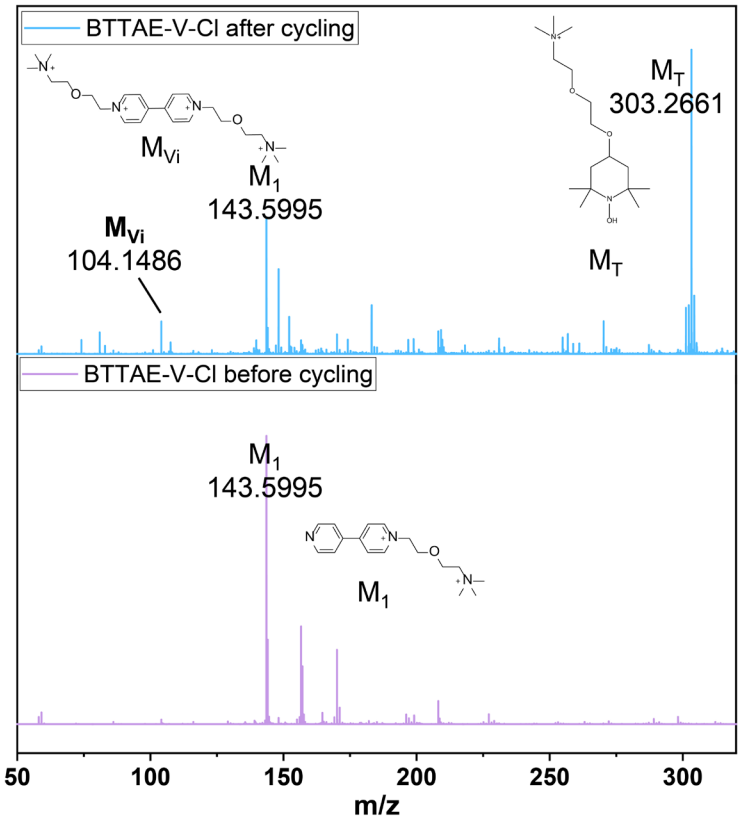

Figure S54 Comparison of LC–MS spectra of BTTAE-V-Cl anolyte before and after cycling in an asymmetric cell with BTTAE-V-Cl as the capacity-limiting side.

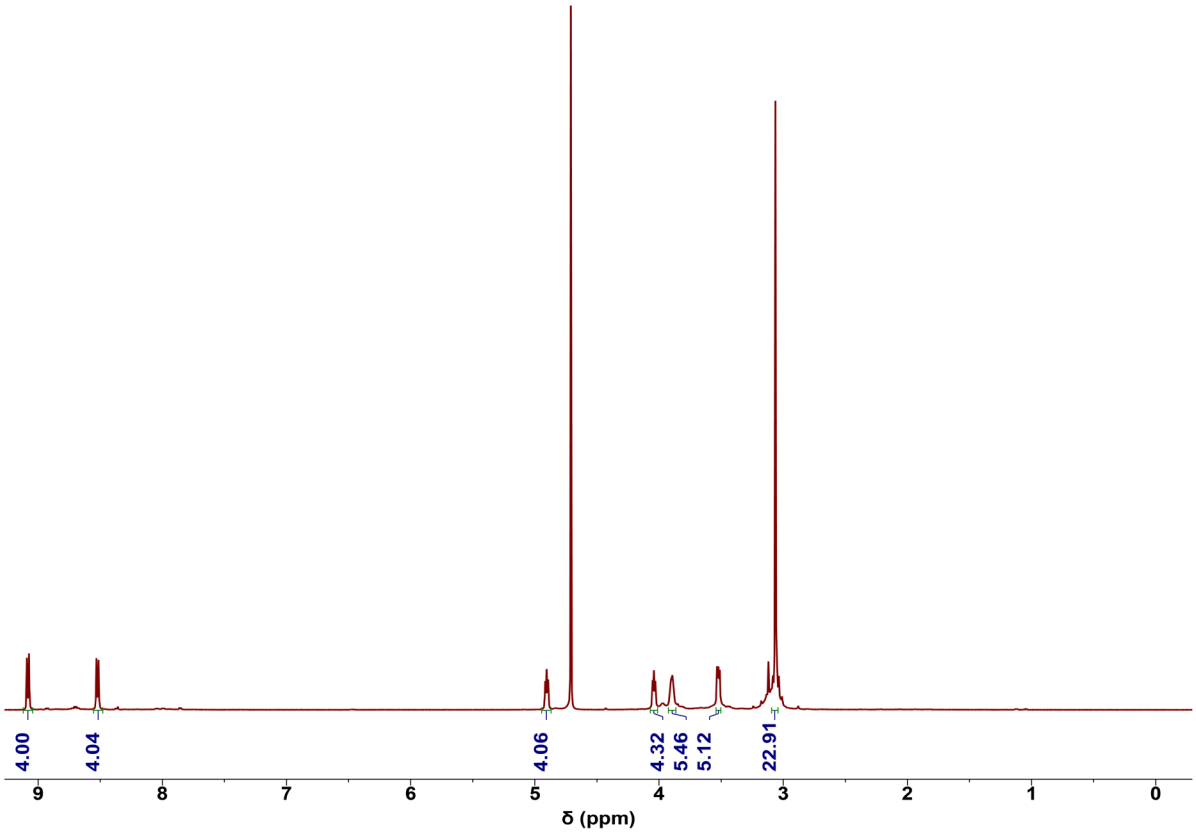

Figure S55 ^{1}H NMR spectrum (400 MHz, D_2O) of BTTAE-V-Cl collected from the anolyte reservoir after flow battery cycling.

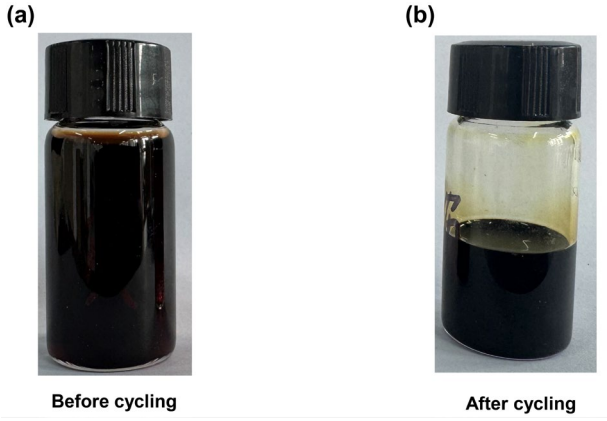

Figure S56 Photographs of the anolyte reservoir before (a) and after (b) high-concentration cycling. The initial electrolyte compositions were 0.5 M BTTAE-V-Cl in 2.0 M NaCl (10 mL) as the anolyte and 1.0 M TMEE-TEMPO-Cl in 2.0 M NaCl (10 mL) as the catholyte. The flow battery was operated under galvanostatic charge–discharge conditions at a current density of 40 mA cm^{-2} within a voltage window of 0.1–1.7 V using a DSV separator.

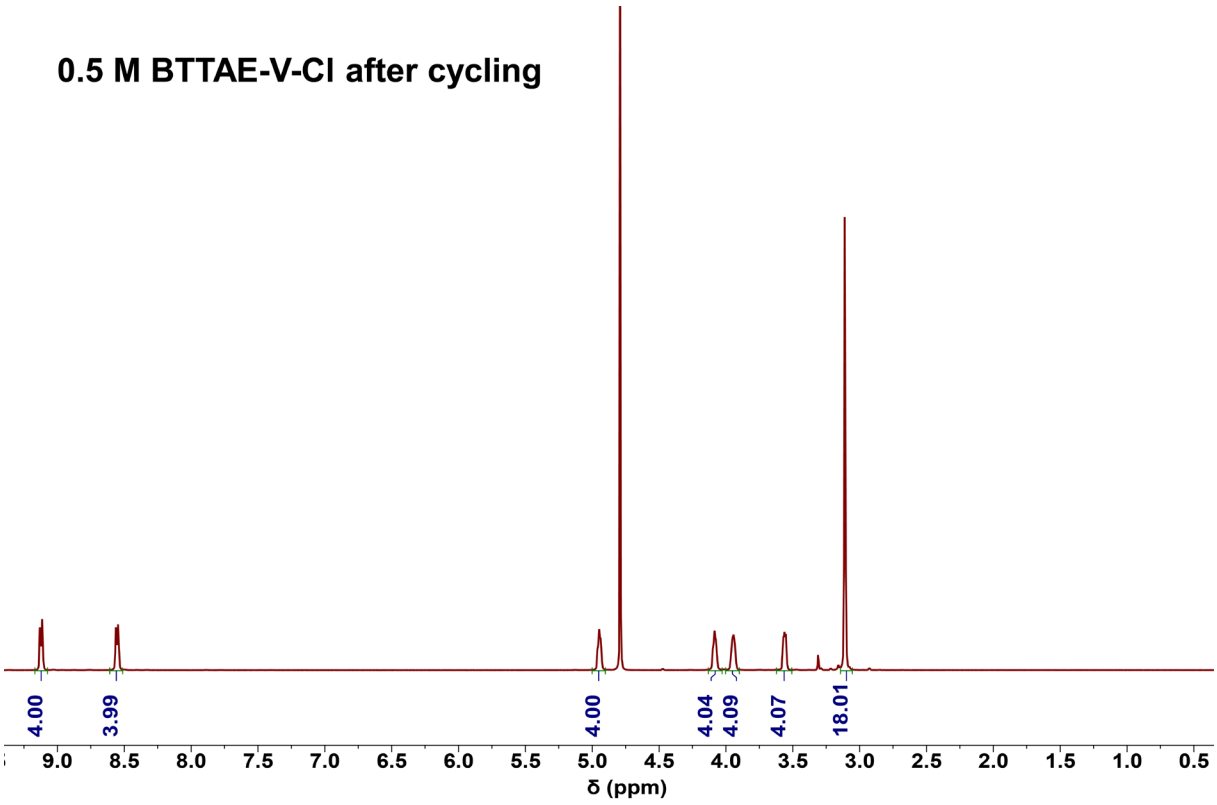

Figure S57 ^{1}H NMR spectrum (400 MHz, D_2O) of 0.5 M BTTAE-V-Cl collected from the anolyte reservoir after high-concentration flow battery cycling.

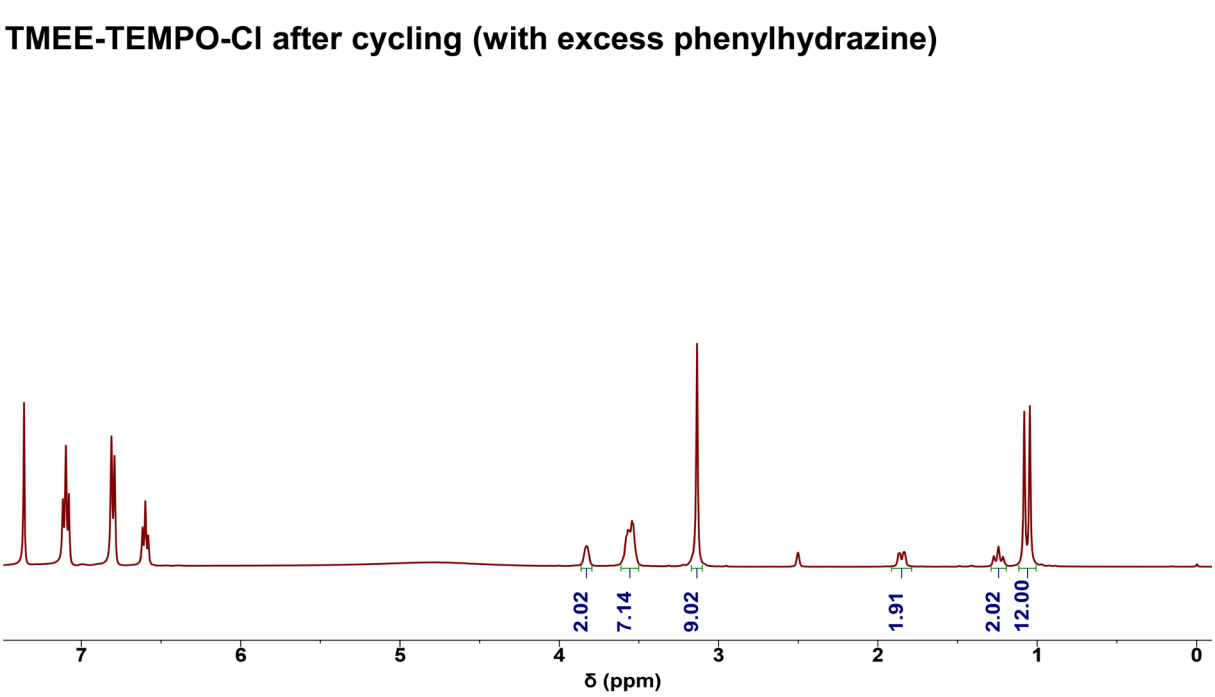

Figure S58 ^{1}H NMR spectrum (400 MHz, DMSO-d_6) of 1.0 M TMEE-TEMPO-Cl collected from the catholyte reservoir after high-concentration flow battery cycling, recorded in the presence of excess phenylhydrazine as a reducing agent.

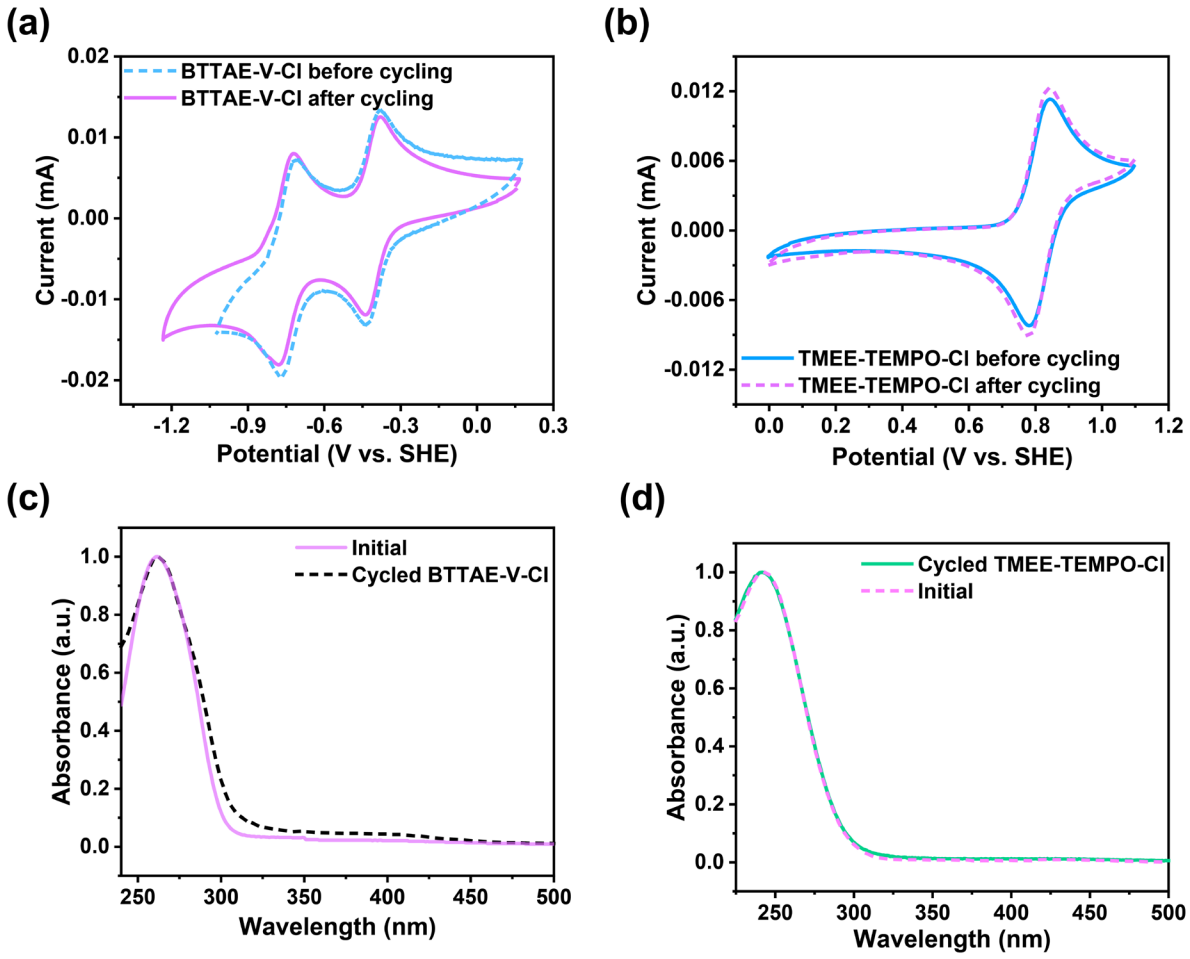

Figure S59 Structural and electrochemical stability of BTTAE-V-Cl and TMEE-TEMPO-Cl electrolytes after high-concentration cycling. (a, b) UV-vis absorption spectra of (a) BTTAE-V-Cl and (b) TMEE-TEMPO-Cl in the pristine state and after high-concentration cycling. (c, d) Cyclic voltammograms of (c) BTTAE-V-Cl and (d) TMEE-TEMPO-Cl recorded at a scan rate of 100 mV s^{-1} before and after high-concentration cycling.

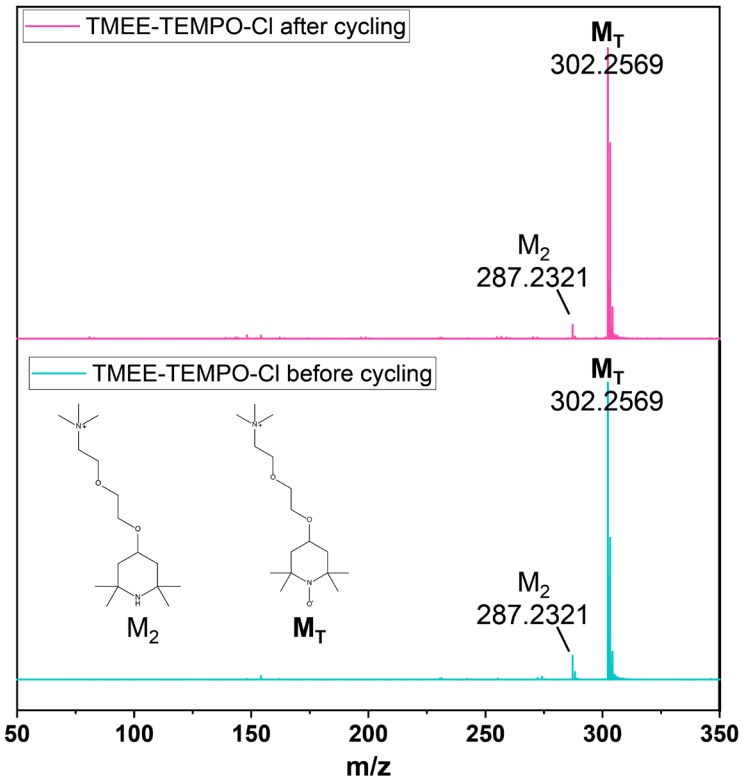

Figure S60 Comparison of LC–MS spectra of TMEE-TEMPO-Cl catholyte before and after high-concentration flow battery testing.

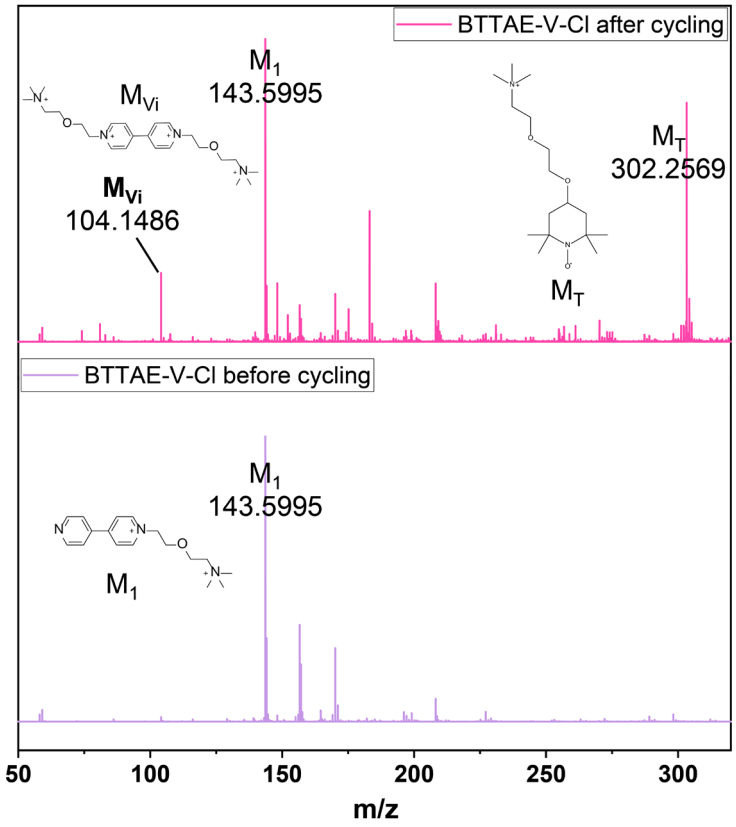

Figure S61 Comparison of LC–MS spectra of BTTAE-V-Cl anolyte before and after high-concentration flow battery testing.

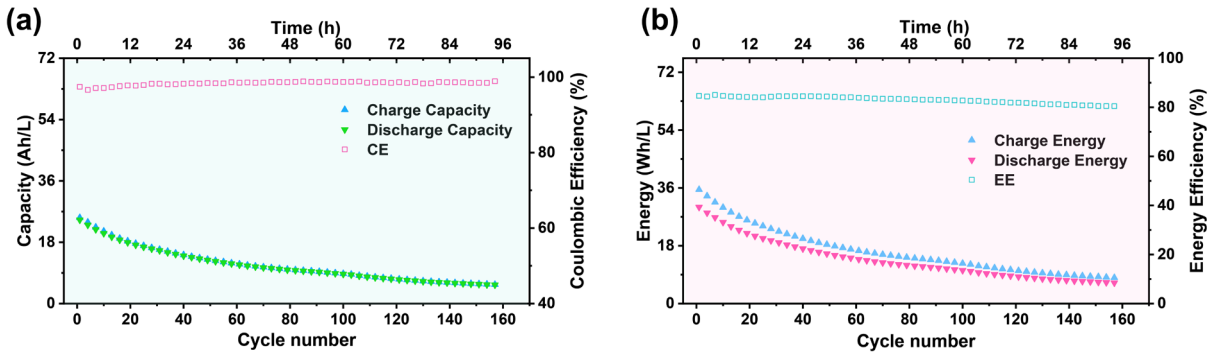

Figure S62 Galvanostatic–potentiostatic (GP) cycling performance of the high-concentration BTTAE-V-Cl/TMEE-TEMPO-Cl flow battery. (a) Charge/discharge capacity and CE as a function of cycle number. (b) Charge/discharge energy and EE during cycling. The battery was operated using 0.5 M BTTAE-V-Cl as the anolyte and 1.0 M TMEE-TEMPO-Cl as the catholyte in 2.0 M NaCl supporting electrolyte. Charging and discharging were performed at 40 mA cm^{-2} within a voltage window of 0.2–1.7 V, followed by a potentiostatic hold at 1.7 V until the current decreased to 2 mA cm^{-2}.

3. Table

Table S1 Comparison of the Solvation Free Energies (ΔG_solv) of BTTAE-V-Cl, TMEE-TEMPO-Cl and their reference molecules.

Molecule	Δ G_solv (kcal mol^{-1})
BTTAE-V^{2+}	**-150.1**
BBrEE^{0}	-15.9
TMEE-TEMPO^{2+}	**-153.3**
M_2^{+}	-62.9

Table S2 Comparison of the Maximum Solubilities of BTTAE-V-Cl and other representative viologen derivatives.

Electrolyte	Water Solubility (mol L^{-1})	Refs
$(CE)_2V$	0.8	[1]
$[PyrPV]Cl_4$	1.13	[2]
$[(NPr)_2TTz]Cl_4$	1.3	[3]
Vi-OEG_3	1.4	[4]
$[(NPr)_2PV]Cl_4$	1.29	[5]
BPP-Vi	1.23	[6]
$[(OHPr)_2TV]Cl_2$	1.44	[7]
PEABP/PESBP	0.6	[8]
BBPE-Vi	1.45	[9]
$(PPBPy)Br_2$	1.1	[10]
M-bisV	1.19	[11]
exBP-Me	1.1	[12]
$(SPr)_2V$	1.4	[13]
BTTAE-V-Cl	**1.55**	**This work**

Table S3 Comparison of the Maximum Solubilities of TMEE-TEMPO-Cl and other representative TEMPO derivatives.

Electrolyte	Water Solubility (mol L^{-1})	Ref
4-OH-TEMPO	2.1	[14]
4-COONa-TEMPO	2.5	[15]
MMA-TEMPO	2.29	
PyrA-TEMPO	2.36	[16]
DMA-TEMPO	2.23	
TPP-TEMPO	2.3	[17]

DFTEMPO	1.9	[18]
N_2-TEMPO	3.0	[19]
N+TEMPOD	2.1	[20]
N+N+TEMPOD	1.5	
TMP-TEMPO	2.4	[21]
Y-TEMPO	1.8	[22]
PSS-TEMPO	2.55	[10]
MIAcNH-TEMPO	2.3	[23]
TMEE-TEMPO-Cl	**3.3**	**This work**

Table S4 Summary of the Electrochemical and Kinetic Properties of BTTAE-V-Cl and other representative viologen derivatives.

Electrolyte	D ($cm^2\ s^{-1}$)	k_0 ($cm\ s^{-1}$)	$E_{1/2}$ (V versus SHE)	Ref
MV	2.57×10^{-5}	2.8×10^{-4}	−0.45 V	[14]
BTMAP-Vi	3.3×10^{-6}	1.4×10^{-2}	−0.358 V	[24]
BHOP-Vi	5.26×10^{-6}	1.12×10^{-2}	−0.433 V	[25]
BPP-Vi	2.7×10^{-6}	2.9×10^{-3}	−0.462 V	[6]
R-Vi	6.97×10^{-6}	1.67×10^{-1}	−0.55 V	[26]
$[(NPr)_2PV]Cl_4$	2.76×10^{-6}	1.98×10^{-2}	−0.76 V	[27]
$(ATBPy)Cl_4$	3.3×10^{-6}	2.8×10^{-3}	−0.55V, −0.75 V	[28]
ex-BPDMe	4.2×10^{-6}	2.03×10^{-3}	−0.81 V	[12]
Dex-Vi	2.3×10^{-6}	5.0×10^{-2}	−0.32 V, −0.70 V	[29]
$[PyrPV]Cl_4$	4.07×10^{-6}	1.42×10^{-2}	−0.76 V	[2]
$(PPBPy)Br_2$	3.91×10^{-6}	2.67×10^{-3}	−0.80 V	[10]
Diquat	4.6×10^{-6}	6.4×10^{-3}	−0.40 V	[30]
BTMAE-Vi	3.6×10^{-6}	1.2×10^{-2}	−0.4 V, −0.74 V	[31]
BTMEP-Vi	2.84×10^{-6}	1.51×10^{-2}	−0.34 V, −0.70 V	[32]
$[PyrTMAV]Cl_4$	3.85×10^{-6}	2.15×10^{-2}	−0.34 V, −0.68 V	[21]
PEABP	3.63×10^{-7}	1.32×10^{-3}	−0.3 V, −0.7 V	[8]
SulEstC1-αViO	3.74×10^{-6}	5.5×10^{-3}	−0.54 V	[33]
$[(NPr)_2SV]Cl_4$	2.83×10^{-6}	7.0×10^{-3}	−0.29 V	[34]
M-bisV	3.18×10^{-6}	1.3×10^{-2}	−0.29 V	[11]
TMAP-bisV	2.58×10^{-6}	1.6×10^{-2}	−0.25 V	
BTTAE-V-Cl	**3.3×10^{-6}** **3.7×10^{-6}**	**1.6×10^{-6}** **2.1×10^{-6}**	**−0.41 V, −0.75 V**	**This work**

Table S5 Summary of the Electrochemical and Kinetic Properties of TMEE-TEMPO-Cl and other representative derivatives.

Electrolyte	D (cm^2 s^{-1})	k_0 (cm s^{-1})	$E_{1/2}$ (V versus SHE)	Ref
4-OH-TEMPO	2.95×10^{-5}	4.5×10^{-4}	+0.8 V	[14]
TEMPTMA	4.8×10^{-6}	4.2×10^{-3}	+0.93 V	[35]
SO_4-TEMPO	2.98×10^{-6}	1.91×10^{-3}	+0.81 V	[36]
MIO-TEMPO	6.35×10^{-6}	1.34×10^{-2}	+0.84 V	[37]
TMAP-TEMPO	3.48×10^{-6}	1.02×10^{-2}	+0.81 V	[38]
CO_2Na-TEMPO	5.45×10^{-6}	2.1×10^{-2}	+0.80 V	[15]
MIAcNH-TEMPO	1.15×10^{-5}	1.86×10^{-2}	+0.83 V	[23]
PSS-TEMPO	3.36×10^{-6}	5.29×10^{-3}	+0.805 V	[10]
N+TEMPOD	8.35×10^{-7}	1.43×10^{-2}	+0.96 V	[20]
DFTEMPO	2.74×10^{-6}	1.53×10^{-2}	+0.806 V	[18]
TMP-TEMPO	4.12×10^{-6}	1.65×10^{-3}	+0.98 V	[21]
TPP-TEMPO	3.39×10^{-6}	5.37×10^{-3}	+0.77 V	[17]
Y-typeTEMPO	6.78×10^{-6}	3.02×10^{-2}	+0.85 V	[22]
Pyr-TEMPO	4.07×10^{-6}	1.42×10^{-2}	+0.81 V	[2]
CT	6.6×10^{-6}	5.78×10^{-3}	+0.8 V	[39]
DMA-TEMPO	6.74×10^{-7}	4.09×10^{-3}	+0.865 V	[16]
TMEE-TEMPO-Cl	**4.1×10^{-6}**	**3.3×10^{-2}**	**+0.81 V**	**This work**

References

1 T. Janoschka, N. Martin, M. D. Hager, U. S. Schubert, *Angew. Chem. Int. Ed*., 2016, **55**, 14427.

2 M. Pan, L. Gao, J. Liang, P. Zhang, S. Lu, Y. Lu, J. Ma, Z. Jin, *Adv. Energy Mater*., 2022, **12**, 2103478.

3 J. Luo, B. Hu, C. Debruler, T. L. Liu, *Angew. Chem. Int. Ed*., 2018, **57**, 231.

4 Y. Yao, W. Ma, J. Lei, Z. Wang, Y-C Lu, L. Liu, *J. Mater. Chem. A,* 2023, **11**, 12984.

5 M. Pan, Y. Lu, S. Lu, B. Yu, J. Wei, Y. Liu, Z. Jin, *ACS Appl. Mater. Interfaces*, 2021, **13**, 44174.

6 S. Jin, E. M. Fell, L. Vina-Lopez, Y. Jing, P. W. Michalak, R. G. Gordon, M. J. Aziz, *Adv. Energy Mater*., 2020, **10**, 2000100.

7 X. Liu, X. Zhang, G. Li, S. Zhang, B. Zhang, W. Ma, Z. Wang, Y. Zhang, G. He, *J. Mater. Chem. A*, 2022, **10**, 9830.

8 E. Grignon, J. Liu, Y. Tan, Y. Cao, A. Aspuru-Guzik, D. S. Seferos, *J. Am. Chem. Soc*., 2025, **147**, 5071.

9 G. Gonzalez, A. A. Nechaev, V. A. Peshkov, E. Martínez-González, A. Belyaev, A. Hamza, M. Shahsavan, P. M. Pihko, P. Peljo, *Chem. – Eur. J*., 2025, **31**, e202404122.

10 M. Gao, M. Salla, Y. Song, Q. Wang, *Angew. Chem. Int. Ed*., 2022, **61**, e202208223.

11 G. Tang, K. Peng, Y. Liu, J. Fang, W. Wu, Z. Yang, T. Xu, *Angew. Chem. Int. Ed*., 2025, **64**, e202501458.

12 G. Tang, Y. Liu, Y. Li, K. Peng, P. Zuo, Z. Yang, T. Xu, *JACS Au*, 2022, **2**, 1214.

13 J. Luo, B. Hu, C. Debruler, Y. Bi, Y. Zhao, B. Yuan, M. Hu, W. Wu, T. L. Liu, *Joule*, 2019, **3**, 149.

14 T. Liu, X. Wei, Z. Nie, V. Sprenkle, W. Wang, *Adv. Energy Mater*., 2016, **6**, 1501449.

15 B. Liu, C. W. Tang, H. Jiang, G. Jia, T. Zhao, *ACS Sustainable Chem. Eng*., 2021, **9**, 6258.

16 Y. Zhao, X. Liu, Z. Wang, J. Huang, J. Huang, X. Deng, X. Zhang, H. Zhang, H. Yu, Y.-K. Li, G.-L. Hou, G. He, *Angew. Chem. Int. Ed*., 2025, **64**, e202512613.

17 G. Tang, W. Wu, Y. Liu, K. Peng, P. Zuo, Z. Yang, T. Xu, *Nat. Commun*., 2025, **16**, 47.

18 L.-C. Yu, Y.-C. Luo, W. Feng, S. Zhang, X. Zhang, *J. Mater. Chem. A*, 2023, **11**, 18911.

19 B. Hu, M. Hu, J. Luo, T. L. Liu, *Adv. Energy Mater*., 2022, **12**, 2102577.

20 X.-L. Lv, P. T. Sullivan, W. Li, H.-C. Fu, R. Jacobs, C.-J. Chen, D. Morgan, S. Jin, D. Feng, *Nat. Energy,* 2023, **8**, 1109.

21 M. Pan, Zh. Jin, T. Zhao, J. Sun, Z. You, E. P. Delmo, M. Farhadpour, Z. Wu, M. Shao, *Chem. Eng. J*., 2024, **496**, 153504.

22 H. Fan, R. Mahalingam, H. Li, Y. Lv, J. Song, *Angew. Chem. Int. Ed*., 2025, **64**, e202504932.
23 H. Fan, B. Hu, H. Li, M. Ravivarma, Y. Feng, J. Song, *Angew. Chem. Int. Ed*., 2022, **61**, e202115908.
24 E. S. Beh, D. D. Porcellinis, R. L. Gracia, K. T. Xia, R. G. Gordon, M. J. Aziz, *ACS Energy Lett*., 2017, **2**, 639.
25 Y. Liu, Y. Li, P. Zuo, Q. Chen, G. Tang, P. Sun, Z. Yang, T. Xu, *ChemSusChem*, 2020, **13**, 2245.
26 H. Li, H. Fan, B. Hu, L. Hu, G. Chang, J. Song, *Angew. Chem. Int. Ed.,* 2021, **60**, 26971.
27 S. Hu, T. Li, M. Huang, J. Huang, W. Li, L. Wang, Z. Chen, Z. Fu, X. Li, Z. Liang, *Adv. Mater*., 2021, **33**, 2005839.
28 M. Huang, S. Hu, X. Yuan, J. Huang, W. Li, Z. Xiang, Z. Fu, Z. Liang, *Adv. Funct. Mater.* **2022**, *32*, 2111744.
29 X.-L. Lv, P. Sullivan, H.-C. Fu, X. X. Hu, H. Liu, S. Jin, W. Li, D. Feng, *ACS Energy Lett*., 2022, **7**, 2428.
30 J. Huang, Z. Yang, V. Murugesan, E. Walter, A. Hollas, B. Pan, R. S. Assary, I. A. Shkrob, X. Wei, Z. Zhang, *ACS Energy Lett*., 2018, **3**, 2533.
31 K. Peng, P. Sun, Z. Yang, T. Xu, *Batteries & Supercaps*, 2023, **6**, e202200426.
32 Y. Liu, D. Hong, J. Wu, Z. Shen, R. Gao, J. Liu, Z. Liu, X. Zhang, X. Han, J. Ran, *ACS Omega*, 2025, **10**, 18641.
33 S. Hwang, M. Oh, K.-J. Lee, C.-S. Jin, S.-K. Park, C. Seo, S.-H. Yeon, D. H. Kim, D. Gueon, Y.-K. Han, K.-H. Shin, *ACS Appl. Mater. Interfaces*, 2024, **16**, 28645.
[34] X. Liu, C. Bao, Z. Wang, C. Liu, X. Zhang, S. Yang, Y.-K. Li, G.-L. Hou, N. Yan, G. He, *Energy Storage Mater*., 2024, **73**, 103824.
35 O. Nolte, P. Rohland, N. Ueberschaar, M. D. Hager, U. S. Schubert, *J. Power Sources*, 2022, **525**, 230996.
36 J. Winsberg, C. Stolze, A. Schwenke, S. Muench, M. D. Hager, U. S. Schubert, *ACS Energy Lett*., 2017, **2**, 411.
37 N.-U. Seo, K. Kim, J. Yeo, S. J. Kwak, Y. Kim, H. Kim, M. Song, K. Choi, Y. Jung, J. Chae, J. Chang, J.-H. Yang, *J. Mater. Chem. A*, 2023, **11**, 18953.
38 Y. Liu, M.-A. Goulet, L. Tong, Y. Liu, Y. Ji, L. Wu, R. G. Gordon, M. J. Aziz, Z. Yang, T. Xu, *Chem*, 2019, **5**, 1861.
39 B. Hu, H. Fan, H. Li, M. Ravivarma, J. Song, *Adv. Funct. Mater*., 2021, **31**, 2102734.